

Impact of Coupled Radiation and Ablation on the Aerothermodynamics of Meteor Entries

Christopher O. Johnston*

NASA Langley Research Center, Hampton, VA 23681 USA

and

Eric C. Stern†

NASA Ames Research Center, Moffett Field, CA 94035

A high-fidelity approach for simulating the aerothermodynamic environments of meteor entries is developed. Two primary components of this model are coupled radiation and coupled ablation. Coupled radiation accounts for the impact of radiation on the flowfield energy equations, while coupled ablation explicitly models the injection of ablation products within the flowfield and radiation simulations. For a meteoroid with a velocity of 20 km/s, coupled radiation reduces the stagnation point radiative heating by over 60%. For altitudes below 40 km, the impact of coupled radiation on the flowfield structure is shown to be fundamentally different, as a result of the large optical thicknesses, than that seen for reentry vehicles, which do not reach such altitudes at velocities greater than 10 km/s. The impact of coupled ablation (with coupled radiation) is shown to provide at least a 70% reduction in the radiative heating relative to the coupled-radiation-only cases. This large reduction is partially the result of the low ionization energies, relative to air species, of ablation products. The low ionization energies of ablation products, such as Mg and Ca, provide strong photoionization and atomic line absorption in regions of the spectrum that air species do not. MgO and CaO are also shown to provide significant absorption. Turbulence is shown to impact the distribution of ablation products through the shock-layer, which results in up to a 100% increase in the radiative heating downstream of the stagnation point. To create a database of heat transfer coefficients, the developed model was applied to a range of cases. This database considered velocities ranging from 14 to 20 km/s, altitudes ranging from 20 to 50 km, and nose radii ranging from 1 to 100 m. The heat transfer coefficients from these simulations are below 0.045 for the range of cases (with turbulence), which is significantly lower than the canonical value of 0.1.

Nomenclature

C_H	Heat transfer coefficient, dimensionless
$h\nu$	Photon energy, eV
I_ν	Frequency-dependent radiative intensity, W-s/cm ² /sr
j_ν	Frequency-dependent emission coefficient, W-s/cm ³ /sr
\dot{m}	Ablation rate, kg/m ² /s
M	Total meteoroid mass, kg
p_w	Surface pressure, Pa
q_{conv}	Convective heating, W/cm ²
q_{Planck}	Planck function for blackbody radiative flux, W/cm ²
q_{rad}^+	Shock-directed radiative flux, W/cm ²
q_{rad}^-	Wall-directed radiative flux, equal to q_{rad} when evaluated at the surface, W/cm ²
q_{rad}	Shock-layer radiative heating, W/cm ²

*Aerospace Engineer, Aerothermodynamics Branch, AIAA Member.

†Research Engineer, Thermal Protection System Materials Branch, AIAA Member.

Q	Heat of ablation, J/kg
R_N	Meteoroid nose radius, m
S_{rad}	Divergence of the radiative flux, W/cm ³
S	Meteoroid cross-sectional area, m ²
T_w	Wall temperature, K
U	Free-stream velocity, km/s
z	Distance along body normal line or normal grid line, cm
α	Absorptivity
ϵ	Emissivity
κ_ν	Absorption coefficient, cm ⁻¹
ν	Frequency, s ⁻¹
ρ	Free-stream density, kg/m ³
θ	Angle from the stagnation point
τ_ν	Optical thickness, dimensionless
<i>Subscript</i>	
ν	Indicates frequency dependence

I. Introduction

This paper presents the extension of a high-fidelity aerothermodynamic simulation model, developed originally for the analysis of reentry vehicles,¹ to the analysis of meteor entries. Whereas the aerothermodynamic analyses of reentry vehicles aim to accurately predict bondline temperatures for the thermal protection system,² the aerothermodynamic analyses of meteors aim to accurately predict the object's mass loss rate due to ablation.³ This mass loss rate is a factor in determining the meteor trajectory and disintegration, which allow for the threat of a meteoroid with a given size, entry velocity, entry angle, and composition to be assessed.^{4,5} The mass loss rate is written as follows:

$$\frac{dM}{dt} = -C_H \frac{S\rho U^3}{2Q} \quad (1)$$

where M is the total mass of the meteoroid, C_H is the heat transfer coefficient, S is the cross-sectional area, U is the free-stream velocity, and Q is the heat of ablation. The heat of ablation is typically assumed to equal values around 8.26 MJ/kg.⁶ This equation shows that the primary quantity of interest from the aerothermodynamic simulation of a meteor is the heat transfer coefficient (C_H). Assuming a spherical geometry for the meteoroid, which will be assumed throughout this paper, C_H is written as:³

$$C_H = \frac{2 \int_0^{\pi/2} q_{rad} \sin\theta d\theta}{\frac{1}{2}\rho U^3} \quad (2)$$

where θ is the angle from the stagnation point, q_{rad} is the radiative heating as a function of θ , and ρ is the free-stream density. This equation assumes convective heating is negligible relative to radiative heating, which is true for all cases considered in this work that include coupled ablation. This equation also shows that an accurate simulation of q_{rad} along the meteoroid surface is required for an accurate prediction of C_H . The ultimate goal of the present work is to provide high-fidelity simulated values of C_H for a range of meteor entry conditions.

Because meteors experience higher entry velocity and slower deceleration than reentry vehicles, they reach lower altitudes at higher velocities. For example, the velocity of the Chelyabinsk meteor⁷ at 30 km altitude was nearly 20 km/s, while the fastest crewed reentry vehicle (Apollo lunar-return) had decelerated to 1.5 km/s by this altitude (down from an initial velocity of 10.8 km/s).⁸ This combination of a high velocity at a low altitude results in higher shock-layer radiative heating and surface ablation rates than encountered for reentry vehicles. The increased importance of shock layer radiation and surface ablation requires that the simulated meteor flowfield include the coupled impact of radiation and ablation, which both will be shown to have a significant impact on q_{rad} or C_H . Although treating coupled radiation and ablation for reentry vehicles has recently become more common,⁹ the magnitude of the coupling is significantly less than for a meteor. As a result, the present work will develop a coupled radiation and ablation approach capable of simulating highly

coupled meteor conditions. Furthermore, the composition of meteoroids include many elements that are not found in the ablator of a reentry vehicle. The resulting species from these additional elements require new flowfield chemistry and radiation models. Note that a recent study by Park,¹⁰ which developed an inviscid stagnation line analysis with coupled ablation, provides significant guidance in developing these new models.

This paper is separated into two primary sections, where the first considers coupled radiation and the second considers coupled ablation. The first of these sections, Section II, begins by presenting details of the coupled radiation flowfield simulation. It then examines the impact of nose radii and altitude on the coupled radiation influence, as well as the impact of the radiative precursor. Similarly, the second of these sections, Section III, begins by presenting details of the coupled ablation flowfield and radiation models. It then examines the impact of coupled ablation on q_{rad} , and shows the influence of turbulence. Finally, Section IV applies the full coupled radiation and ablation model developed in the previous two sections to create a database of C_H values. This database considers nose radii between 1 and 100 m, altitudes between 20 and 50 km, and velocities between 14 and 20 km/s. Note that recent work by Dias et al.¹¹ focuses on nose radii below the 1 m lower limit of the present study.

II. Impact of Coupled Radiation

As mentioned in the Introduction, the potential of meteors to reach altitudes below 50 km, while maintaining velocities above 14 km/s, makes the treatment of coupled radiation essential for simulating accurate radiative heating values. Details of the coupled radiation model developed for this analysis are presented in subsection A. Subsection B then examines the impact of coupled radiation on a meteor flowfield, as well as identifies unique features of coupled radiation meteor flowfields that are not seen for more commonly studied reentry vehicles. Finally, subsection C examines the impact of the free-stream gas absorbing shock layer radiation, also referred to as precursor absorption.

A. Flowfield and Radiation Modeling for Coupled Radiation

This work applies the LAURA v5 Navier-Stokes solver.¹² Because altitudes below 60 km are considered here exclusively, along with nose radii of 1 m or greater, the impact of thermal nonequilibrium is expected to be small. As a result, a single temperature model is applied (except for the study of precursor absorption, for which a two-temperature model is required). However, chemical nonequilibrium is treated to allow the present models to be applied to wake simulations in the future (only the front, or forebody, of the sphere is considered in this work). For the present cases without ablation, the following 13 species are treated in the flowfield: N, N⁺, N⁺⁺, O, O⁺, O⁺⁺, N₂, N₂⁺, O₂, O₂⁺, NO, NO⁺ and e⁻. Thermodynamic properties for N, N⁺, N⁺⁺, O, O⁺, and O⁺⁺ are obtained from the high-temperature curve fits developed by Johnston et al.¹ For the remaining species, the thermodynamic properties are obtained from Gordon and McBride.¹³ The transport properties are obtained from Wright et al.^{14,15} where available. The remaining species are treated using the approximate approach of Svehla¹⁶ modified as suggested by Park.¹⁷ An axisymmetric hemisphere grid with 128 points in the body normal direction and 32 points along the surface was applied for all cases.

All radiation computations are made using the HARA radiation code.¹⁸ For air species, HARA applies a comprehensive set of radiation properties, including spectral data and non-Boltzmann models for diatomic molecules and atomic species, which were critically assessed and chosen in studies by Johnston et al.^{19,20} The accuracy of HARA's predictions for high temperature air, at conditions relevant to meteor shock layers, has been assessed through comparisons with shock tube measurements.^{21–23} These studies show that measurements and HARA simulations agree within 30% at equilibrium conditions.

Coupled radiation refers to a flowfield computed with the divergence of the radiative flux (S_{rad}) included in the flowfield energy equations.²⁴ This is in contrast to the uncoupled radiation approach, where the flowfield is computed with S_{rad} set to zero, followed by the radiative heating being computed (from this flowfield) as a post-processing step. Therefore, in the uncoupled approach the flowfield computation is completely uncoupled from the radiation computation. Because of the significant impact of S_{rad} on the flowfield, this uncoupled approach will be shown to be unacceptable for meteor entry conditions.

For coupled radiation, the divergence of the radiative flux is written for a point z in the flowfield as

$$S_{rad,\nu}(z) = 4\pi j_{\nu}(z) - \kappa_{\nu}(z) \int_{4\pi} I_{\nu} d\psi \quad (3)$$

where the first term represents the emitted energy and the second term represents the energy absorbed from the incoming radiation from the surrounding flowfield. A recent study by Johnston and Mazaheri²⁵ shows that the second term in this equation may be accurately approximated by the tangent-slab approximation, which reduces the computational cost of evaluating this term by two orders-of-magnitude. The tangent-slab approximation, which is applied in this work, assumes one-dimensional radiative transport along body-normal rays through the shock layer. This approximation allows S_{rad} to be written as

$$S_{rad,\nu}(z) = \frac{d(q_{rad,\nu}^+ - q_{rad,\nu}^-)}{dz} \quad (4)$$

where $q_{rad,\nu}^+$ and $q_{rad,\nu}^-$ are the shock- and wall-directed radiative flux. Note that the value of $q_{rad,\nu}^-$ at $z=0$ is the radiative heating.

To avoid numerical instabilities, S_{rad} is typically set to zero in the free-stream. This approach will be applied for the coupled radiation simulations presented in this work, except for the study of precursor absorption in Section IIC. To model precursor absorption, the radiation computation is extended into the free-stream. Furthermore, photochemical source terms computed in HARA, resulting from photoionization and photodissociation, are coupled to the flowfield species continuity equations. Additional details regarding the photochemical source terms and precursor absorption, along with their impact on the radiative heating, are presented in Section IIC.

The typical impact of including this S_{rad} term is the reduction of the shock layer temperatures relative to the uncoupled values, which is the result of radiative emission reducing the total enthalpy of the shock layer.²⁶ Because meteoroids tend to reach lower altitudes at higher velocities than reentry vehicles, and because of the potential larger size of a meteoroid, the optical thickness of a meteoroid shock layer can be significantly larger than for a reentry vehicle. This larger optical thickness results in a fundamentally different S_{rad} distribution through the shock layer, which changes the resulting coupled radiation temperature distribution.²⁷ Examples of this behavior are presented in the following paragraphs.

B. Impact of Coupled Radiation on Stagnation Line

Figure 1(a) compares the uncoupled and coupled stagnation line temperatures for a case with a velocity of 20 km/s and altitude of 30 km. Results for both a radius of 10 m and 30 m are presented. The impact of coupled radiation is seen reduce the temperatures through the layer similarly for both nose radii. Furthermore, coupled radiation is seen to increase the boundary layer thickness dramatically for both cases. Note that these thicker boundary layers are due purely to coupled radiation, and not viscosity. These coupled radiation boundary layers will be discussed further in the following paragraphs. Figure 1(b) shows that because this boundary layer is thicker for the 30 m case, it is able to provide more absorption for q_{rad}^- . The resulting q_{rad}^- values at the wall are 38 and 28 W/m² for the 10 and 30 m cases, respectively. The coupling ratio (coupled/uncoupled radiative heating) is 0.20 and 0.16 for the 10 and 30 m cases, respectively, which shows that the impact of coupled radiation increases (corresponding to a lower coupling ratio) slightly with increasing nose radius.

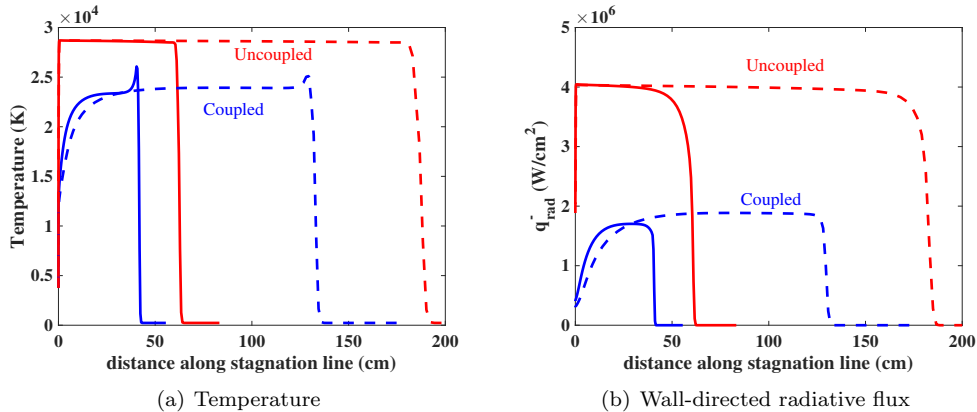


Figure 1: Impact of increasing nose radius (R_N) on coupled radiation impact (Solid lines: $R_N=10$ m, Dashed lines: $R_N=30$ m).

In addition to the impact of varying nose radius on coupled radiation, varying the free-stream density or altitude has a significant impact on the coupled radiation behavior. For altitudes above 40 km, the shock layer is not optically-thick at 20 km/s, meaning S_{rad} is nonzero across the layer and q_{rad}^- is below the Planck function (q_{Planck}). This behavior is similar to that seen for reentry vehicles. Figure 2 presents an example of this regime, which consists of a 10 m radius case at 20 km/s and an altitude of 50 km. Figure 2(a) confirms the nonzero S_{rad} values through the middle of the layer for the uncoupled case. These nonzero values lead to the continuous decrease in temperatures, moving from the shock to the wall, shown in Fig. 2(b) for the coupled case. Figure 2(c) shows that these decreased temperatures for the coupled case result in an 80% reduction in q_{rad}^- reaching the surface. This figure also confirms that q_{rad}^- is well below q_{Planck} throughout the inviscid region of the flow for both the coupled and uncoupled cases, which is consistent with the nonzero S_{rad} values. Close to the surface, however, q_{rad}^- becomes larger than q_{Planck} , which is the result of the sharp decreasing temperature gradient.

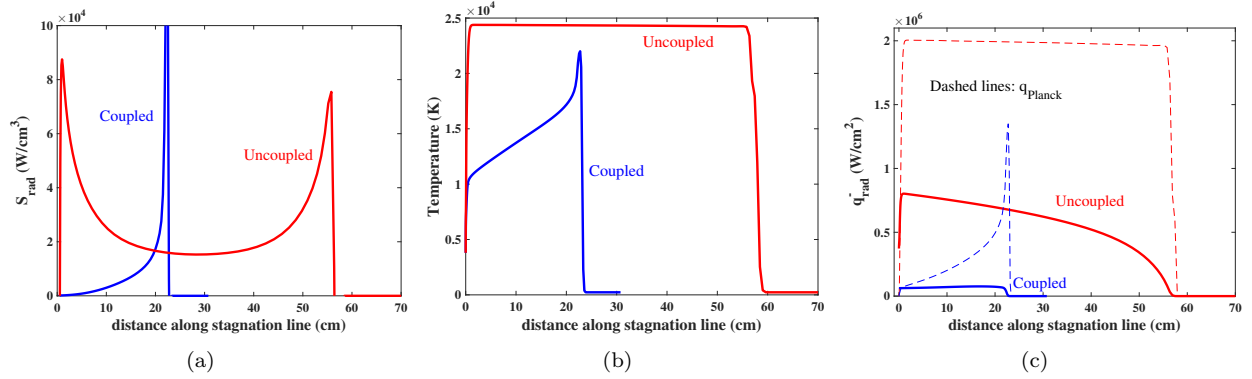


Figure 2: Impact of coupled radiation for a case at with a velocity of 20 km/s, altitude of 50 km, and nose radius of 10 m.

For altitudes below 40 km, the shock layer becomes optically-thick at 20 km/s, meaning S_{rad} approaches zero near the middle of the layer and q_{rad}^- reaches q_{Planck} . Figure 3 presents an example of this regime, for a 10 m radius case at 20 km/s and an altitude of 30 km. Note that this case is the same as that in the previous paragraph, except the altitude has been lowered from 50 to 30 km. Figure 3(a) confirms that S_{rad} approaches zero throughout the middle of the shock layer for the uncoupled case. As shown in Figure 3(b), the nonzero S_{rad} values concentrated near the shock and wall lead to temperature gradients near the shock and wall for the coupled case. The temperatures through the center of the layer are nearly constant due to the local S_{rad} values near zero. This regime of coupled radiation, where the temperature gradients are limited to narrow regions near the shock and wall, is not seen in the study of reentry vehicles. Recall that although these temperature gradients appear to be the result of a thick viscous boundary layer and post-shock nonequilibrium region, they are actually due to the radiation coupling, and specifically to the fact that S_{rad} approaches zero in the middle of the shock layer. Although this behavior has been discussed in previous studies by Goulard²⁷ and Biberman,²⁸ it has not previously been studied with modern shock-capturing flowfield codes.

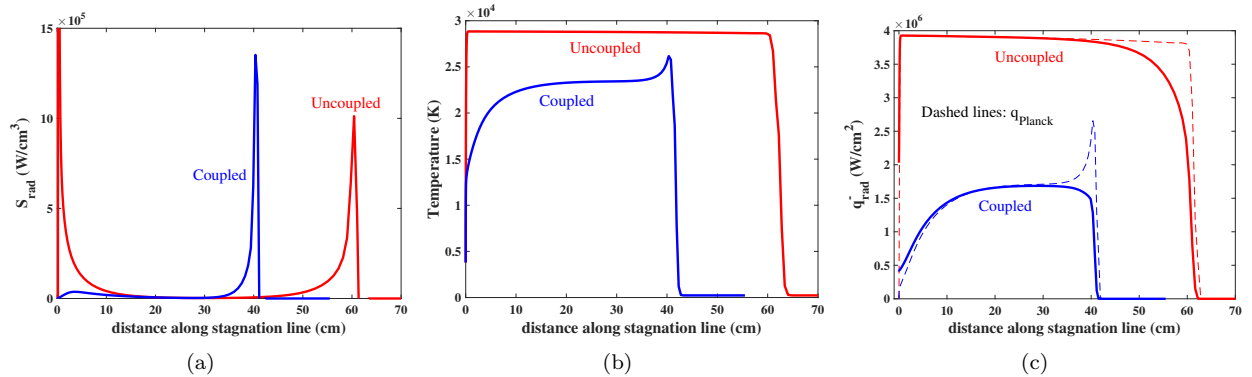


Figure 3: Impact of coupled radiation for a case at with a velocity of 20 km/s, altitude of 30 km, and nose radius of 10 m.

To summarize the present discussion regarding the impact of nose radius and altitude on the impact of coupled radiation, Fig. 4(a) presents the ratio of coupled to uncoupled radiative flux for a range of nose radii and altitudes, all with a velocity of 20 km/s. This figure confirms that the impact of coupled radiation increases with increasing nose radius for all cases, regardless of the optical thickness. The increasing impact of coupling with increasing altitude is the result of the decreased optical thickness at higher altitude, which allow for the nonzero S_{rad} values across the layer. This trend can also be seen by comparing Figs. 2 and 3.

Figure 4(b) presents the stagnation-point radiative heating values for the 20 km/s cases. This figure shows that for the non-optically-thick conditions at 50 km, increasing the nose radius increases the radiative heating. Conversely, for the optically-thick cases at 20 and 30 km altitudes, the radiative heating decreases with increasing nose radius. Recall that this decrease with increasing radius is due to the larger coupled wall layer shown in Fig. 1. The increased radiative heating with increasing radius is the typical trend seen for non-optically-thick reentry vehicles, where the larger shock-standoff distance provides a larger path length of radiating gas.

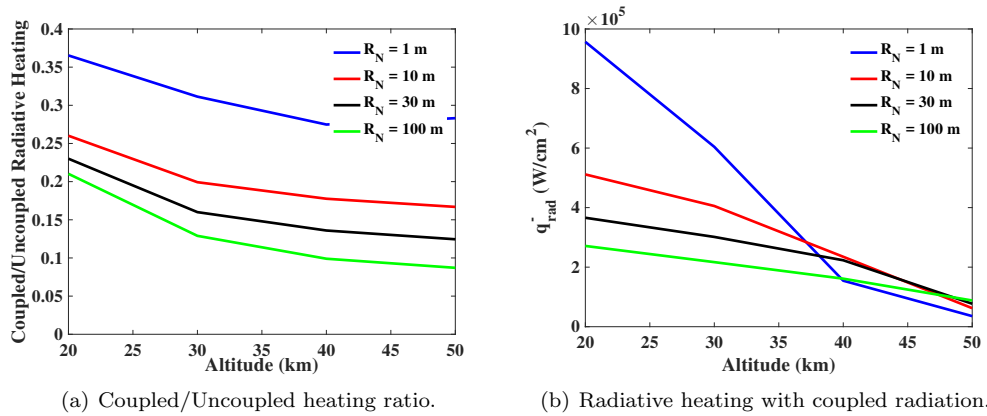


Figure 4: Stagnation point coupled radiation values at 20 km/s.

C. Impact of Precursor Absorption

The preceding coupled radiation analysis assumed the radiative flux leaving the shock layer was not absorbed in the free-stream gas, therefore, ignoring any precursor absorption impact. This assumption was enforced by setting S_{rad} to zero ahead of the shock, which was detected when temperatures fell below 2000 K. This assumption is typically applied for coupled radiation simulations for four primary reasons. First, to sufficiently model the precursor, the computational grid must extend far into the free-stream (at least the distance of 10 shock layer thicknesses). This slows down both the flowfield and radiation solutions. Second, radiation and two-temperature flowfield modeling of the low temperature free-stream gas contains significant uncertainty. Third, photochemical chemical processes, such as photodissociation and photoionization, have a significant impact on the flowfield species continuity equations in the precursor. This increased importance of photochemical source terms in the precursor is due to collisional processes being weakened by the low free-stream number densities. Computing the photochemical source terms requires additional solutions of the radiative transport equations, which slows down the simulation. Fourth, a two-temperature model is required in the precursor, even if the shock layer is in strong thermochemical equilibrium, which further slows down convergence.

Johnston et al.²⁹ considered the precursor impact for a 5 m radius sphere at 15 km/s and an altitude of 60 km. This study found a radiative heating increase of 20% due to treating the precursor. A similar increase of 15% was reported later by Johnston et al.¹ for a 1 m radius sphere at 22 km/s and an altitude of 60 km. The model applied for these studies is presented in Johnston et al.,¹⁸ which contains the photochemical processes listed in Table 1. Not only do these processes provide the dominant absorption for the free-stream gas, which impact the precursor temperatures through S_{rad} , but they also noticeably impact the species continuity equations as a photochemical source term. In addition to applying the processes listed in Table 1, the precursor model also requires a correction to S_{rad} to account for the non-tangent-slab geometry of the precursor as the distance from the shock layer increases. This correction, which was developed by Stanley

and Carlson,³⁰ is applied as follows:

$$S_{rad,\nu} = \frac{dq_{rad,\nu}^-}{dz} + \phi_\nu \frac{dq_{rad,\nu}^+}{dz} \quad (5)$$

Following Stanley and Carlson,³⁰ the correction factor ϕ_ν is written as

$$\phi_\nu = 1 - \cos^2 \beta \frac{0.5 - E_3(\tau_\nu \sec(\beta))}{0.5 - E_3(\tau_\nu)} \quad (6)$$

where E_3 is the third exponential integral, τ_ν is the optical depth computed from the wall to the point in the precursor. The angle β is one-half of the angle subtended by the body, computed as

$$\beta = \sin^{-1} \frac{R_N + z_s}{R_N + z} \quad (7)$$

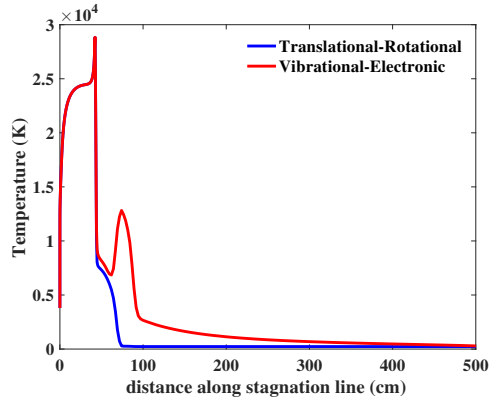
where R_N is the nose radius of the meteoroid, z_s is the shock standoff, and z is the distance along the body normal. Equations 6 and 7 are applied for points in the precursor, defined as all points where $z > z_s$. Note that at $z = z_s$ the correction termed ϕ_ν is equal to one, while as z becomes large ϕ_ν goes to zero. Johnston and Mazaheri²⁵ confirmed the accuracy of this approach through the application of a detailed ray-tracing approach.

Table 1: Photochemical Processes Applied in the Present Study.

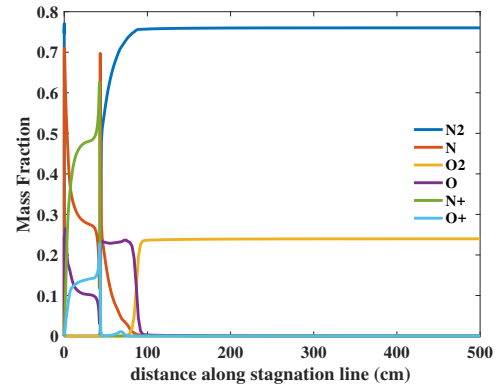
#	Process	Spectral Range	Data Source
1	N ₂ Photodissociation: N ₂ + hν ↔ 2N	9.8 eV < hν	Stanley and Carlson ³⁰
2	O ₂ Photodissociation: O ₂ + hν ↔ 2O	7.1 eV < hν	Mnatsakanyan ³¹
3	N ₂ Photoionization: N ₂ + hν ↔ N ₂ ⁺ + e ⁻	12.4 eV < hν	Romanov et al. ³²
4	O ₂ Photoionization: O ₂ + hν ↔ O ₂ ⁺ + e ⁻	9.7 eV < hν	Romanov et al. ³²
5	N Photoionization: N + hν ↔ N ⁺ + e ⁻	12.4 eV < hν	TOPbase ³³
6	O Photoionization: O + hν ↔ O ⁺ + e ⁻	9.7 eV < hν	TOPbase ³³

To assess the impact of the precursor absorption for conditions relevant to meteors, the precursor model discussed in the previous paragraph was applied to the previously considered 30 and 50 km altitude cases (with a radius of 10 m and velocity of 20 km/s). Figure 5 presents stagnation line properties for the 30 km case. Figures 5(a) and 5(b) show the temperatures and mass fractions along the entire computational range of the stagnation line, which extends 5 m from the nose. The bow shock is located near 45 cm, where the temperature spikes above 25,000 K. Starting from the outer boundary at 500 cm and moving toward the shock, the vibrational-electronic temperature rises gradually until 100 cm (due to absorption). A negligible change in the mass fractions is seen up to this point. Immediately below 100 cm, O₂ dissociates completely and N₂ begins to dissociate, while the vibrational-electronic temperature rises rapidly to a peak at 75 cm. Below this point, ionization of O becomes significant, which provides electrons to begin equilibrating the two temperatures (through electronic-translational energy relaxation³⁴). This thermal equilibration reduces the vibrational-electronic temperature and increases the translational-rotational temperature until the shock is reached at 45 cm, at which point both temperatures increase. Figures 5(c) and 5(d) compare the temperatures with and without precursor modeling for the first 100 cm away from the surface. For the precursor case, the enthalpy crossing the shock is increased by the free-stream absorption, which results in the higher shock layer temperatures in the outer region of the shock layer. However, because of the optical thickness of the shock layer, where radiation emitted below 10 cm and toward the shock is completely absorbed before it reaches the shock, this region below 10 cm is not influenced strongly by the including the precursor (i.e., S_{rad} in this region is not influenced). This weak precursor influence near the wall results in a negligible change to the temperatures below 10 cm with the addition of the precursor. Although the q_{rad}^- values above 10 cm are higher for the precursor case, the similar temperature profiles below 10 cm result in q_{rad}^- reaching the surface to be within 2%. Note that the precursor may have a significantly larger impact on the radiative flux emitted from the shock layer to a distant observer. This “observed” radiative flux, which will also likely be influenced significantly by the wake, will be the subject of a future study.

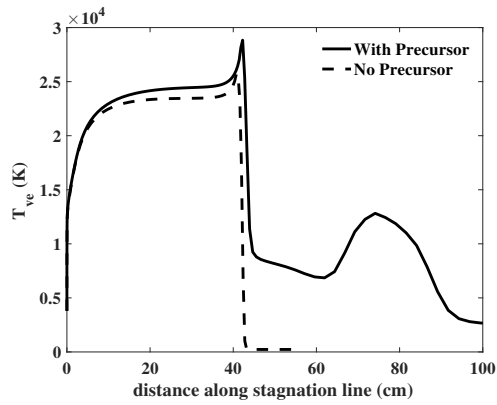
For the 50 km case, Fig. 6 presents the same set of figures as shown for the 30 km case. The temperature profiles presented in Fig. 6(a) show that the vibrational-electronic temperatures remain above 5000 K until



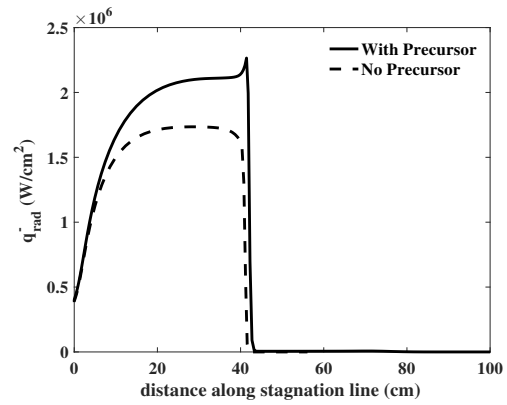
(a)



(b)



(c)



(d)

Figure 5: Precursor simulations for the 30 km altitude case.

a distance of 200 cm, while for the 30 km case this distance was only 100 cm. This larger precursor region for the 50 km case is the result of its lower free-stream density, which is 1% of the 30 km value. This lower free-stream density decreases the optical thickness, which increases the length of free-stream gas required to absorb the radiation emitted from the shock layer. The precursor impact on the first 100 cm of the shock layer for this 50 km case is shown in Fig. 6(c) and Fig. 6(d). Strong absorption near 26 cm leads to a sharp increase in temperature, which provides an increase in q_{rad}^- . At the surface, including the precursor results in a 25% increase in q_{rad}^- . Although the temperatures near the wall are similar for the precursor and no precursor cases, which for the 30 km case resulted in q_{rad}^- values at the wall within 2%, this case is not as optically-thick as the 30 km case, which reduces the impact of the temperatures near the wall on the radiative heating. The 25% increase in the radiative heating seen here may be considered an upper-limit for the precursor influence. Simulations presented in the remainder of this paper do not include the precursor. Note that the significant absorption due to ablation products shown in the next section would likely diminish this 25% precursor influence. This is expected because ablation products will be shown to significantly increase the optical thickness of the boundary layer.

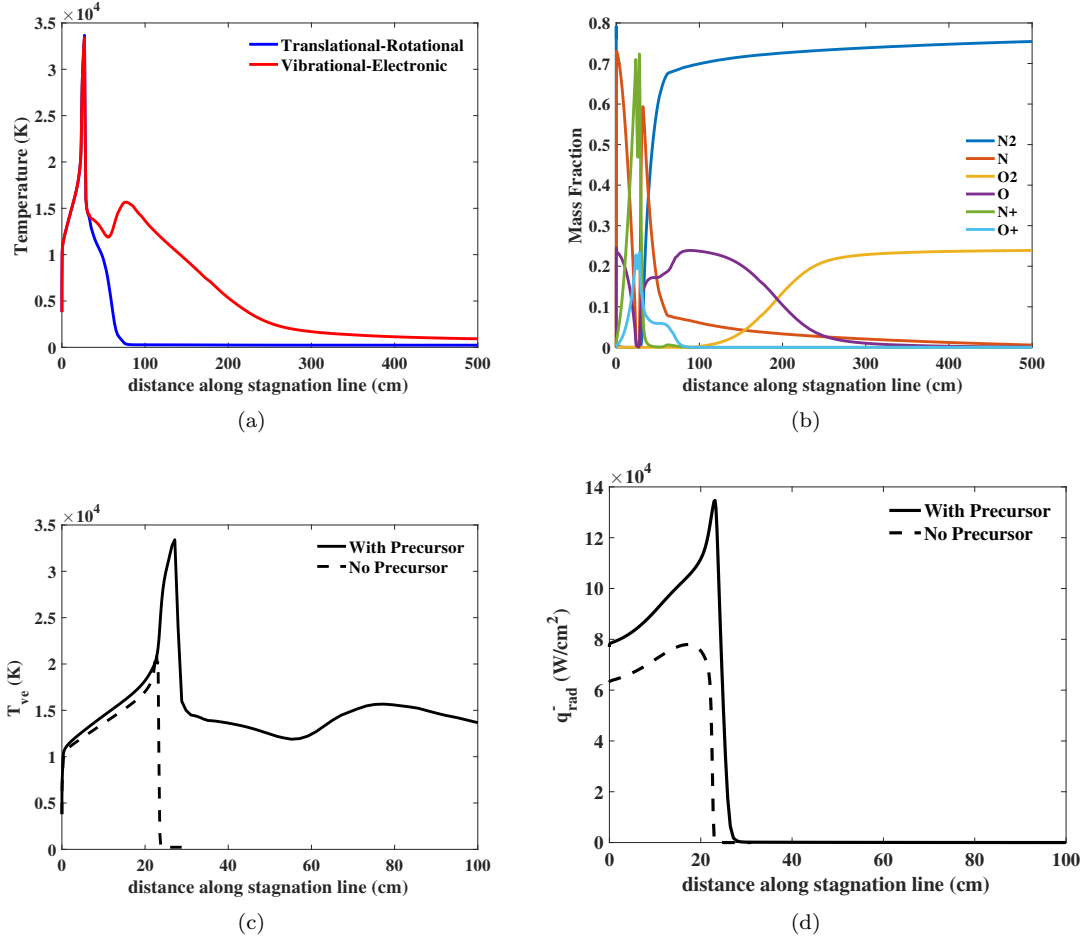


Figure 6: Precursor simulations for the 50 km altitude case.

III. Impact of Coupled Ablation

This section examines the impact of coupled ablation on the radiative heating. Coupled ablation is defined as the modeling of an ablating surface boundary condition within the flowfield computation. As will be shown, this coupled ablation approach is essential for modeling the aerothermodynamic environment of meteors because of their relatively large ablation rates, which significantly alter the structure of the flow near the surface. Furthermore, coupled ablation introduces species into the flow that greatly alter the

radiative environment. The present section investigates this coupled ablation impact by first developing a coupled ablation model appropriate for meteors, which is presented in subsection A. This is followed by the detailed study of two cases in subsection B, which provides insight into the influence of coupled ablation on the flowfield structure and radiative heating. Finally, the impact of turbulence on the coupled ablation environment is investigated in subsection C.

A. Flowfield and Radiation Modeling for Coupled Ablation

The ablating surface boundary condition for this analysis is simplified by the massive ablation present for meteor entries at the conditions of present interest (velocities greater than 12 km/s at altitudes below 50 km). The presence of massive ablation, where the boundary layer is blown off the surface, results in elemental mass fractions at the surface equal to those of the surface material. This is in contrast to weaker ablation cases, such as the diffusion-limited oxidation regime, where the elemental mass fractions at the surface are a combination of the surface material and boundary layer edge gas. With the assumption that the elemental mass fractions at the surface are equal to those of the surface material, the surface temperature and enthalpy may be curve-fit as a function of pressure as follows:

$$T_w = 3021.0 - 209.59\ln(p_w) + 40.097\ln(p_w)^2 - 2.1897\ln(p_w)^3 + 0.057422\ln(p_w)^4 \quad (8)$$

$$h_{abl} = 1.1235 \times 10^7 - 1.7419 \times 10^6 \ln(p_w) + 2.2495 \times 10^5 \ln(p_w)^2 - 1.2814 \times 10^4 \ln(p_w)^3 + 2.7686 \times 10^2 \ln(p_w)^4 \quad (9)$$

where p_w has units of Pa, T_w is in K, and h_{abl} is in kg/m³. The data for these curve-fits were provided by Chen³⁵ for an LL-Chondrite meteoroid. For the surface pressures of interest, h_{abl} has a value of nearly 6.2 MJ/kg. Combining h_{abl} with the heat of fusion, which is approximately 2 MJ/kg, results in a value near the empirically derived 8.26 MJ/kg that is typically applied for Q in Eq. (1). For the present study, h_{abl} considers only ablation due to vaporization, which ignores melting and the heat of fusion. This is a good approximation for the stagnation region of meteoroids with nose radii greater than 1 m, where the melt layer is thin and removed rapidly from the surface (this removal would have a minimal impact on the flowfield because it does not introduce gaseous species). However, for shoulder regions or for smaller meteoroids, removal of melt could have a significant impact on the surface energy balance. This impact is beyond the scope of the present work.

The ablation rate \dot{m} is computed from these curve-fits and the surface energy balance:

$$\dot{m} = \frac{q_{rad}\alpha + q_{conv} - \epsilon\sigma T_w^4}{h_{abl}} \quad (10)$$

where α is the absorptivity and ϵ is the emissivity of the surface, which are both set to unity for this work. Recall that for the present cases, q_{conv} is negligible and $\epsilon\sigma T_w^4$ is less than 15% of q_{rad} . For this equation to be consistent with Eq. (1), C_H should include these additional terms. The C_H values presented later in this work apply Eq. 2, which only includes q_{rad} . The surface species are computed assuming chemical equilibrium at the surface pressure, temperature, and elemental composition.

The elemental mass fractions of the surface material, which represent an LL-Chondrite meteoroid, were assumed as follows:³⁵ O = 0.457, Si = 0.206, Fe = 0.172, Mg = 0.120, Na = 0.005, S = 0.020, Al = 0.010, Ca = 0.010. To account for the addition of these elements to the 13 species air chemistry, the following 26 species were added to the LAURA flowfield simulations: Fe, Fe⁺, FeO, Mg, Mg⁺, MgO, Si, Si⁺, SiO, SiO₂, Fe⁺⁺, Mg⁺⁺, Si⁺⁺, S, S⁺, SO, SO₂, Al, Al⁺, AlO, Ca, Ca⁺, CaO, Na, Na⁺, NaO. The thermodynamic properties for atomic neutrals and ions were computed using electronic levels from NIST, which were also implemented in the HARA radiation computation, to ensure that Saha-Boltzmann and Boltzmann electronic state populations are coincident. This behavior is required to accurately apply nonequilibrium radiation models for these species. Although the current forebody simulations are strongly equilibrated, therefore making negligible the influence of nonequilibrium radiation, future work that will utilize these simulations will include a wake and radiative signature computation, which are strongly influenced by nonequilibrium. Besides atomic neutrals and ions, the thermodynamic properties for the remaining species are taken from Gordon and McBride.³⁶ The flowfield rate model for these species is presented in Table 2. Again, the influence of these rates will primarily be seen in future work, as the present strongly equilibrated forebody simulations are insensitive. Note that the electron-impact ionization rates are based on the rate for atomic nitrogen, which is scaled using the ionization energy. This approach is taken by Park³⁷ to obtain the electron-impact ionization rates commonly applied for C and O.

Solutions of Eqs. (8) - (10) were obtained every 50,000 flowfield solution iterations, and a relaxation factor of 0.3 was applied to the ablation rate. This relaxation factor is required because changing the ablation rate influences the species profiles and temperatures, which impact the radiative heating and S_{rad} distributions.

Except for cases where the precursor is treated in Section IIC, photochemical source terms are not included in the flowfield, because of their added computational expense. For air shock layers, this assumption is common for altitudes below 70 km, where shock layer number densities are relatively high, except in the free-stream or wake. Photochemical source terms have a negligible impact in regions of large number densities because collisional rates scale with number density squared, while photoionization and photodissociation scale linearly with number density. Because the present cases are all at 50 km or lower in altitude, this assumption is expected to remain valid for air species. However, with the introduction of ablation products with low ionization potentials, such as Mg and Ca, this assumption requires a reevaluation. Simulations at 30 and 50 km altitudes were performed with the photoionization source terms from all atomic ablation products. Comparing these results with the cases without the photoionization source terms, the resulting radiative heating values were within 1% for the 30 km case and 2% for the 50 km case. These difference are for the shoulder, or maximum radius location of the sphere, where the disagreement is largest. At the stagnation points the values were within 0.5%. This good agreement indicates that treating the photochemical source terms is not required for forebody simulations at altitudes below 50 km. Therefore, these terms were not included in the other simulations reported in this paper.

Table 2: Chemical kinetics for meteor ablation products.

i	Reaction	$A_{f,i}$	$n_{f,i}$	$D_{f,i}$	Ref.
1	$\text{Si} + \text{e}^- \leftrightarrow \text{Si}^+ + \text{e}^- + \text{e}^-$	2.5e+34	-3.82	9.46e+4	Based on N rate ¹⁷
2	$\text{Fe} + \text{e}^- \leftrightarrow \text{Fe}^+ + \text{e}^- + \text{e}^-$	2.5e+34	-3.82	9.17e+4	Based on N rate ¹⁷
3	$\text{Mg} + \text{e}^- \leftrightarrow \text{Mg}^+ + \text{e}^- + \text{e}^-$	2.5e+34	-3.82	8.87e+4	Based on N rate ¹⁷
4	$\text{Si} + \text{NO} \leftrightarrow \text{SiO} + \text{N}$	3.2e+13	0.0	1775.0	Mick et al. ³⁸
5	$\text{Si} + \text{O}_2 \leftrightarrow \text{SiO} + \text{O}$	2.1e+15	-0.53	16.83	Le Picard et al. ³⁹
6	$\text{SiO} + \text{M} \leftrightarrow \text{Si} + \text{O} + \text{M}$	4.0e+14	0.0	9.56e+4	Estimate
7	$\text{SiO}_2 + \text{M} \leftrightarrow \text{SiO} + \text{O} + \text{M}$	4.0e+14	0.0	9.56e+4	Estimate
8	$\text{Fe} + \text{O}_2 \leftrightarrow \text{FeO} + \text{O}$	1.3e+14	0.0	1.02e+4	Akhmadov et al. ⁴⁰
9	$\text{Mg} + \text{O}_2 \leftrightarrow \text{MgO} + \text{O}$	5.1e+10	0.0	0.0	Hodgson and Mackie ⁴¹
10	$\text{SO} + \text{O} \leftrightarrow \text{S} + \text{O}_2$	2.4e+07	1.51	2.53e+3	Lu et al. ⁴²
11	$\text{SO}_2 + \text{S} \leftrightarrow \text{SO} + \text{SO}$	4.8e+14	0.0	1.08e+4	Murakami ⁴³
12	$\text{O}_2 + \text{SO} \leftrightarrow \text{SO}_2 + \text{O}$	2.3e+12	0.0	3.70e+3	Garland ⁴⁴
13	$\text{Al} + \text{O}_2 \leftrightarrow \text{AlO} + \text{O}$	2.0e+13	0.0	0.0	Cohen and Westberg ⁴⁵
14	$\text{Al} + \text{SO}_2 \leftrightarrow \text{SO} + \text{AlO}$	9.6e+13	0.0	2.00e+3	Fontijn and Felder ⁴⁶
15	$\text{Al} + \text{e}^- \leftrightarrow \text{Al}^+ + \text{e}^- + \text{e}^-$	2.5e+19	-0.82	6.94e+4	Based on N rate ¹⁷
16	$\text{NaO} + \text{O} \leftrightarrow \text{Na} + \text{O}_2$	2.2e+14	0.0	0.0	Plane and Husain ⁴⁷
17	$\text{Na} + \text{e}^- \leftrightarrow \text{Na}^+ + \text{e}^- + \text{e}^-$	2.5e+19	-0.82	5.96e+4	Based on N rate ¹⁷
18	$\text{Ca} + \text{O}_2 \leftrightarrow \text{CaO} + \text{O}$	2.5e+14	0	7.25e+3	Kashireninov et al. ⁴⁸
17	$\text{Ca} + \text{e}^- \leftrightarrow \text{Ca}^+ + \text{e}^- + \text{e}^-$	2.5e+19	-0.82	7.09e+4	Based on N rate ¹⁷

Many of the 26 additional species added to the flowfield to account for meteor ablation products have a significant impact on the shock layer radiation. To account for this impact, radiation models were developed and added to the HARA code. For each neutral atomic species, an atomic line model was developed based on energy levels and line strengths from NIST. For each line, Stark broadening widths were obtained from Griem,⁴⁹ where available, and a correlation¹⁹ otherwise. Atomic line models for ionized species were also developed, but were found to have a negligible influence. Atomic photoionization cross sections for atomic neutrals and ions were obtained from TOPbase.³³ As with atomic lines, only the photoionization from atomic neutrals provide a noticeable impact on the radiative heating. For molecular band systems, Table 3 summarizes the band systems treated and the source of modeling data used for each. Many of these bands system models are based on the work of Park.⁵⁰

To provide insight into the impact of coupled ablation on the shock layer environment, cases at 30 and 50 km altitude will be studied, both with a velocity of 20 km/s and a radius of 10 m. The impact of coupled radiation was presented in the previous section for these two cases. Note that all results presented in the present section include coupled radiation.

Table 3: Summary of molecular band modeling for meteor ablation products.

Specie	Transition	Spectral Range (eV)	Data Source
SiO	A-X	4.54-5.79	Franck-Condon factors and energy levels from Geier et al., ⁵¹ and band oscillator strength from Park and Arnold. ⁵²
SiO	E-X	5.74-7.55	Franck-Condon factors and band oscillator strength taken from Naidu et al. ⁵³ and Drira, ⁵⁴ and energy levels from Lagerqvist. ⁵⁵
FeO	Orange	1.68-2.38	Oscillator strengths and energy levels taken from Michels. ⁵⁶
MgO	B-A	1.72-2.45	Oscillator strengths and energy levels taken from Daily ⁵⁷ and Bell et al. ⁵⁸
MgO	D-A	1.72-2.45	Oscillator strengths and energy levels taken from Naulin et al. ⁵⁹ and Bell et al. ⁵⁸
MgO	B-X	2.38-2.69	Oscillator strengths and energy levels taken from Daily ⁵⁷ and Bell et al. ⁵⁸
CaO	A-X	1.1-2.0	Oscillator strengths and energy levels taken from Doherty ⁶⁰ and Liszt. ⁶¹
CaO	B-X	2.6-3.7	Oscillator strengths and energy levels taken from Pasternack ⁶² and Liszt. ⁶¹
CaO	Orange	1.7-2.2	Oscillator strengths and energy levels taken from Pasternack ⁶² and Liszt. ⁶¹
CaO	Green	1.7-2.2	Oscillator strengths and energy levels taken from Pasternack, ⁶² Liszt, ⁶¹ and Baldwin. ⁶³
SO	A-X	3.8-5.0	Franck-Condon factors and band oscillator strength taken from Borin ⁶⁴ and energy levels from Rosen. ⁶⁵
AlO	B-X	2.2-3.0	Oscillator strengths and energy levels taken from Borovicka. ⁶⁶

B. Impact of Coupled Ablation on the Stagnation Line at 20 km/s

For the high-pressure 30 km case, Fig. 7 presents the stagnation-line temperatures, ablation product mole fractions, and wall-directed radiative flux (q_{rad}^-). For the temperature and q_{rad}^- profiles, comparisons are made between the coupled ablation and no ablation cases (this no ablation case corresponds to the coupled radiation result from the previous section). Considering the temperature profiles in Fig. 7(a), it is seen that coupled ablation increases the shock standoff distance. This increased shock standoff distance is due the mass injection at the surface resulting from ablation, which at the stagnation point is 5.1% of the free-stream mass flux for this case. The size of the ablation layer is apparent from the ablation species mole fractions in Fig. 7(b), which extend roughly 6 cm away from the surface. Figure 7(c) shows that, other than the increase in shock standoff distance, the q_{rad}^- profile is similar for the coupled ablation and no ablation cases, except for near the wall. To clarify this near wall region, Figs. 7(d) - (f) present the first 4 cm away from the wall for the same profiles shown in (a) - (c). These figures of the near wall region show that below 1 cm, the temperatures for the coupled ablation case are lower than for the no ablation case. This region corresponds to a rise in the molecular species SiO, MgO, FeO, and CaO, which are restricted to this near wall region. The impact of these ablation species on q_{rad}^- is seen in Fig. 7(f), where below 2.5 cm q_{rad}^- decreases significantly faster for the coupled ablation case, indicating stronger absorption. This absorption is seen to increase as the wall is approached, which corresponds to an increase in the neutral atomic and molecular mole fractions. The resulting value of q_{rad}^- at the wall is more than an order of magnitude lower for the coupled ablation case (1.3 W/m²) than for the no ablation case (38 W/m²).

To investigate further the more than order-of-magnitude decrease in the radiative flux reaching the wall due to coupled ablation, the q_{rad}^- spectra at four points through the ablation layer are presented in Fig. 8(a). The Planck function is presented for each point as a dashed line. To help interpret each of these spectra, Fig. 8(b) presents the associated absorption coefficient for each case. For distances from the wall (z) above 0.47 cm, the q_{rad}^- spectrum follows the Planck function at the local flowfield temperature. This is the result of the absorption coefficients values above 10 cm⁻¹ across the entire spectrum shown in Fig. 8(b) combined with minor gradients in temperatures and number densities shown in Fig. 7(d) and 7(e). The minor deviations of the q_{rad}^- spectrum from the Planck function for the 0.47 cm case is the result of these gradients. Moving towards the surface to the 0.21 cm point, the deviation from the Planck function increases between 1 and 3 eV. This is due to the increased temperature and number density gradients and decreased absorption coefficients in this spectral range. Moving to the 0.13 cm point, the absorption coefficient below 2 eV is seen to decrease by an order-of-magnitude, which causes a significant deviation between q_{rad}^- and the Planck function. Finally, moving to the wall, the q_{rad}^- values below 2 eV are reduced only slightly from the values at 0.13 cm, which is due to absorption coefficient values below 2 cm⁻¹ over this 0.13 cm thick layer. Above

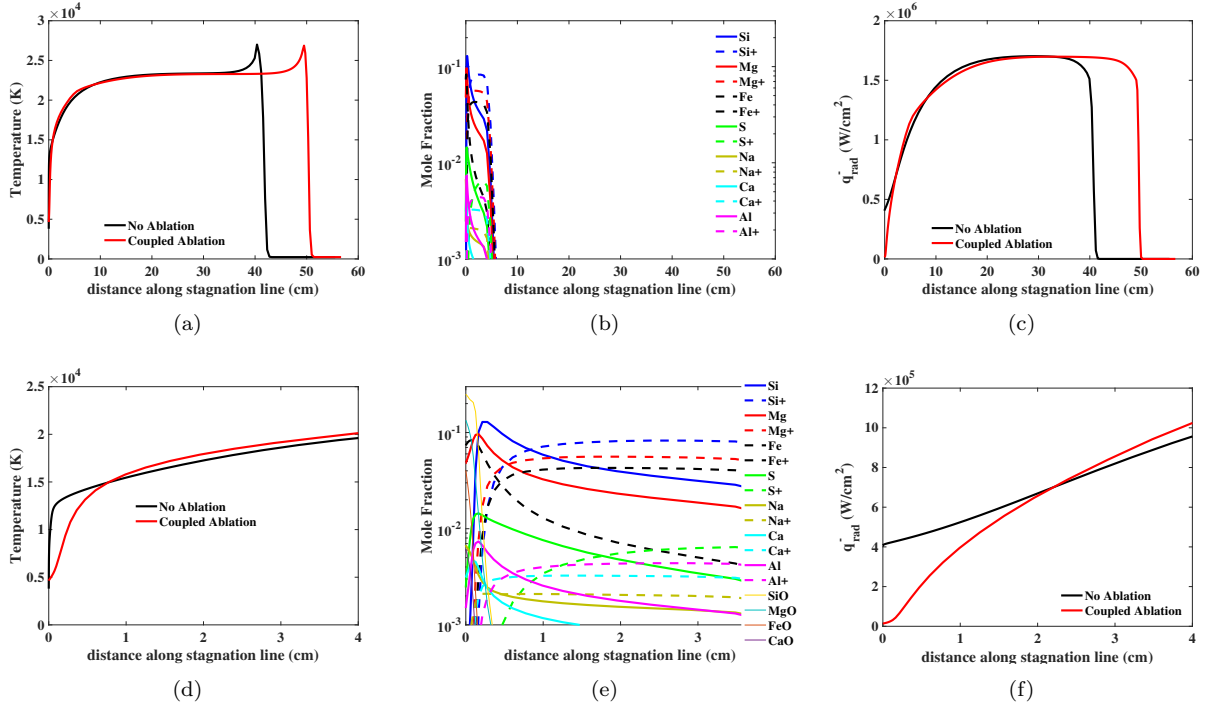


Figure 7: Impact of coupled ablation for the 30 km altitude case.

2 eV, however, the absorption coefficient values greater than 10 cm^{-1} drive most of the q_{rad}^- spectrum down to the Planck function at the wall temperature.

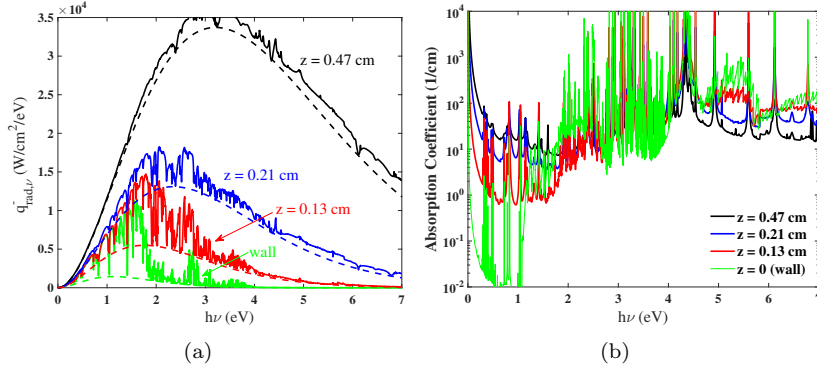


Figure 8: Spectral details at various points along the stagnation line for the 30 km altitude case.

Because of the sensitivity of the q_{rad}^- spectrum on the absorption coefficient spectrum near the wall, it is insightful to separate the absorption coefficient spectrum into its components. This breakdown is presented in Fig. 9 for the 0.47, 0.13, and 0.0 cm points. For each point, the figure on the left presents the contribution from molecular band systems, the middle figure presents the contribution from atomic photoionization, and the figure on the right presents the atomic line contribution. The vertical scales for each of these figures were fixed to those of Fig. 8(b). When combined with the free-free and induced emission contribution, the values in these figures sum to the values presented in Fig. 8(b). These figures show the anticipated result that moving from the higher temperature point at 0.47 cm towards the wall, the atomic line and photoionization contribution decreases and the molecular band contribution increases. Note also that the atomic lines become significantly narrower as the wall is approached due to decreasing electron number densities (which reduce Stark broadening) and decreasing temperatures (which reduce Doppler broadening). Considering the 0.47 cm point, the Mg atomic line contribution below 2 eV is dominant, while above 2 eV the Fe lines provide a similar contribution. The photoionization component at this point is also dominated

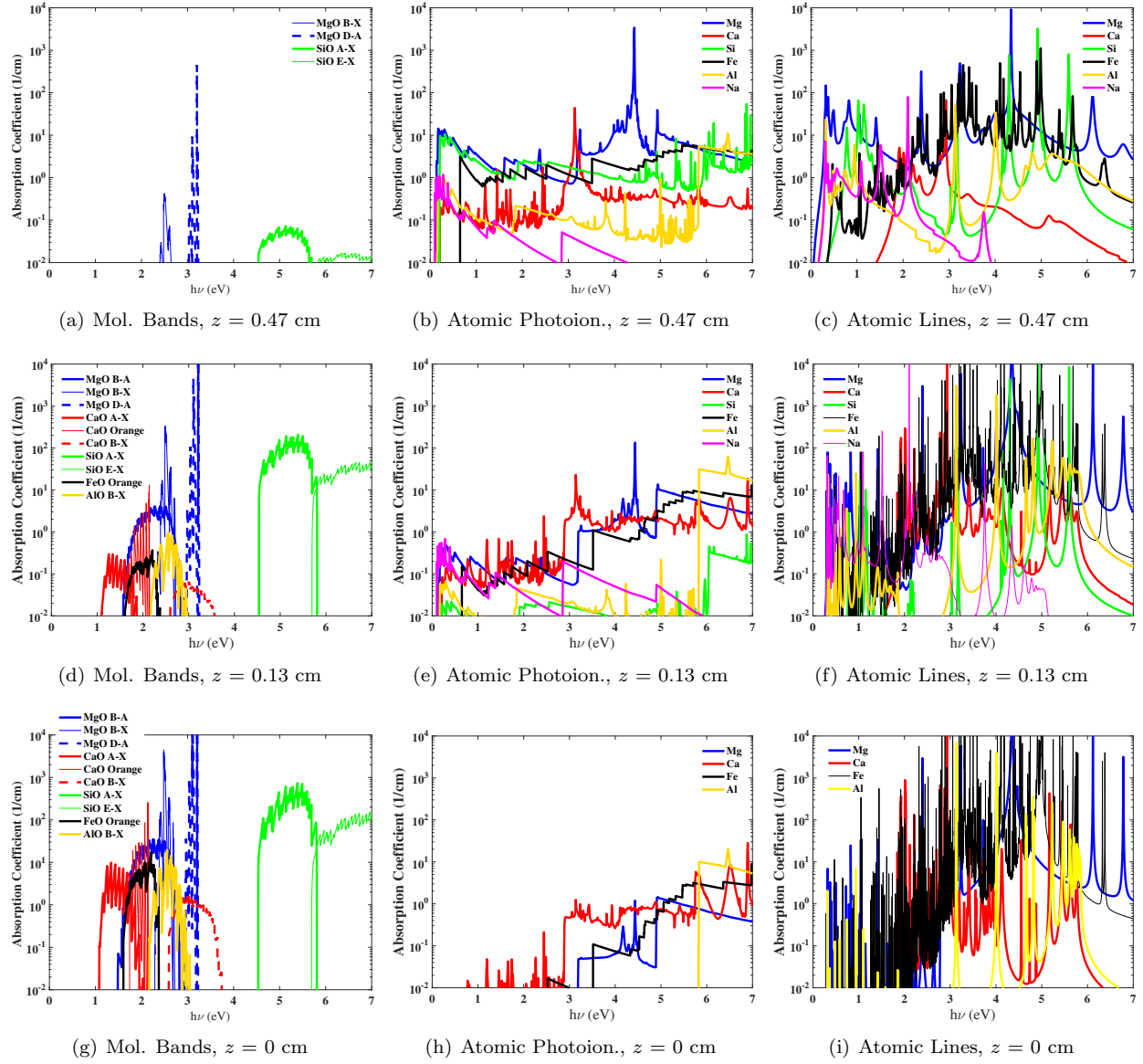


Figure 9: Spectrum components from individual species and radiative processes for the 30 km altitude case.

by Mg, but is lower than the line contribution over most of the spectrum shown here. Because of the low molecular number densities at 0.47 cm, the molecular band absorption coefficients are mostly below the lower limit of the vertical scale, except for a few narrow spikes from MgO and SiO bands. Moving to the 0.13 cm point, the narrower atomic lines remain dominant. The lower temperature at this point decreases the atomic line and photoionization contributions below 2 eV, due to lower populations of the upper electronic levels associated with these transitions. This temperature decrease allows the rising MgO and CaO band systems to provide a noticeable contribution below 2 eV. Finally, at the lower temperature wall, the molecular band contributions increase significantly, due to the increased molecular number densities, while the atomic contributions decrease significantly below 3 eV. Note that the lack of any band system to fill the spectrum below 1 eV causes the sharp drop off in the absorption coefficient at the wall shown in Fig. 8(b). If the ablation product elements considered here were replaced with air elements of N and O, these gaps in the absorption coefficient would cover a significant fraction of the spectrum, due to the negligible atomic line and photoionization contribution for air below 8,000 K. This negligible contribution is the result of the significantly higher ionization energies for N and O, which are 14.53 and 13.62 eV, respectively, compared to the meteor ablation products, which are as low as 5.14 and 6.11 eV for Na and Ca, respectively. This observation is the fundamental reason for the dramatic decrease in the radiative heating for coupled ablation cases relative to the no ablation cases.

To further clarify the impact of each ablation product species and radiative process on the radiative heating, Table 4 lists the percent increase in the radiative heating (q_{rad}^- at the wall) due to setting the absorption and emission coefficient spectrum for individual processes equal to zero (this is done as a post-processing step to a converged coupled radiation and ablation flowfield). Processes that have less than a 0.2% impact are not listed. For the present 30 km altitude case (the 50 km case will be discussed later), the dominant atomic processes are provided by Mg, as anticipated from Fig. 9. Although Fe lines appear to be stronger than Ca lines in this figure, the location of the Fe lines coincide closely with Mg, while the peak Ca lines are located near 2 eV, where other processes are weak. This explains the Ca line contribution of 10.5%, which is slightly larger than the Fe contribution of 9.71%. This also emphasizes that although the absorption coefficient for an individual process may be large (greater than 10 cm^{-1}) over a wide region of the spectrum, it will not result in a large sensitivity in Table 4 if it overlaps with another process of similar or greater strength. This is because once a spectral region is completely optically thick, meaning $q_{rad,\nu}^-$ is equal to the local Planck function, increasing the absorption coefficient further does not change $q_{rad,\nu}^-$.

Table 4: Percent increase in stagnation point radiative flux due to removing individual radiative processes.

Specie	Mechanism	30 km	50 km
Fe	Lines	9.71	4.11
Mg	Lines	22.5	32.1
Si	Lines	1.58	1.27
Ca	Lines	10.5	5.62
Fe	Photoionization	1.75	2.51
Mg	Photoionization	3.60	6.41
Si	Photoionization	0.71	1.27
Al	Photoionization	0.16	0.32
Ca	Photoionization	1.61	3.53
Na	Photoionization	0.64	1.10
MgO	B-A	22.9	25.1
MgO	D-A	1.25	1.00
MgO	B-X	2.10	0.56
SiO	A-X	0.65	0.14
FeO	Orange	2.78	2.30
AlO	B-X	1.51	2.76
CaO	A-X	10.1	25.4
CaO	B-X	0.38	0.77
CaO	Orange	2.22	1.43

To investigate the impact of coupled ablation on the lower pressure case at 50 km altitude, Fig. 10 compares the stagnation line temperatures and q_{rad}^- values for the coupled ablation and no ablation cases. Also presented are the ablation product mole fractions, which are only available for the coupled ablation case. Unlike for the 30 km case, where the shock stand-off increased by 25% with coupled ablation, the

shock stand-off is seen to increase by over 100% for this case. This difference is due to the stagnation point ablation rate being 5.1% of the free-stream mass flux for the 30 km case, while it is 51% of the free-stream mass flux for this 50 km case (even though the dimensional ablation rate is 40% lower for the 50 km case, the free-stream density is 18 times lower). The ablation product mole fractions indicate the ablation layer extends roughly 27 cm away from the body, which causes the significant increase in the shock standoff distance. Absorption from this ablation layer reduce the q_{rad}^- value at the surface by 88%.

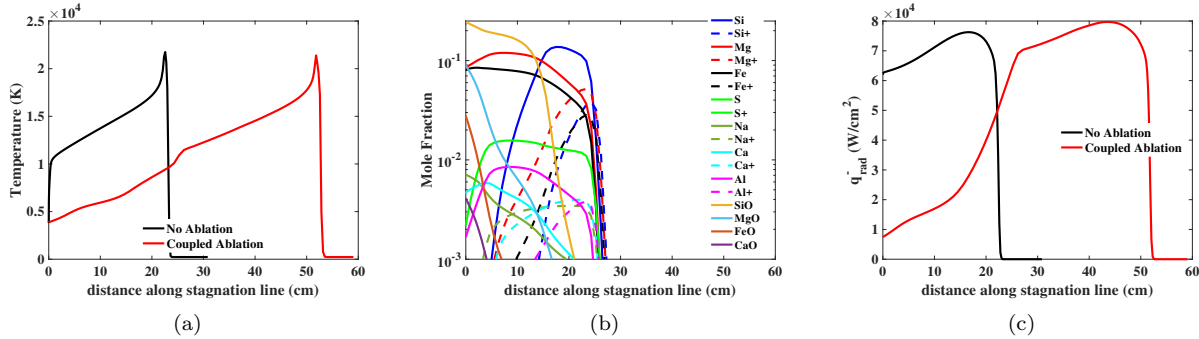


Figure 10: Impact of coupled ablation for the 50 km altitude case.

To provide further details of this 88% reduction, Fig. 11 presents the radiative flux and absorption coefficient spectra at four locations along the stagnation line. Starting at the edge of the ablation layer at 27.1 cm, which contains essentially all air species, it is seen that much of the q_{rad}^- spectrum remains below the local Planck function (represented by the dashed line). This was shown previously in Fig. 2 for the no ablation case. Although the temperature is 11,680 K for this point, which is higher than the other three points considered, the resulting absorption coefficient spectrum is significantly lower above 1 eV than the other points. This is a consequence of this 27.1 cm point containing all air species. This is confirmed by next considering the 22.5 cm point, which is dominated by atomic ablation species. The absorption coefficient increases by more than an order-of-magnitude over most of the spectrum, which drives the q_{rad}^- spectrum closer to the local Planck function. The individual components of the absorption coefficient are presented in Fig. 12(a) - (c) for this point. Atomic lines and photoionization from Mg and Si are dominant below 2 eV, while above this other atoms contribute noticeably. As shown in Fig. 10, the region of the ablation layer dominated by atomic species ranges from 10 to 27 cm, while molecular species dominate closer to the wall. The 4.6 cm point shown in Fig. 11 represents this molecular dominated region. The significantly reduced atomic line and photoionization contributions result in decreased absorption coefficients below 2 eV. Figures 12(d) - (f) show the details of this drop-off, which are offset slightly by the increased molecular band contribution. Note that the atomic lines shown in Fig. 12(f), which are difficult to interpret, are too narrow to provide significant absorption. Moving finally to the surface, most of the q_{rad}^- spectrum above 2 eV that remains at 4.6 cm is absorbed due to the MgO band systems, while between 1 and 2 eV the CaO A-X band system absorbs a noticeable amount. Below 1 eV the q_{rad}^- spectrum remains unchanged between 4.5 cm and the wall, due the absorption decrease in this spectral region.

To summarize the observations made in the previous paragraph, Table 4 lists the percent change in q_{rad}^- at the wall due to removing individual processes. The most significant processes are seen to be Mg lines, MgO B-A, and CaO A-X. Recall that these processes provide not only large absorption coefficients, but are also located in regions of the spectrum that do not overlap other strong processes. This explains the relatively small sensitivities seen for overlapping photoionization processes, such as Mg, Fe, and Si, even though they contribute large absorption coefficients.

To generalize the impact of coupled ablation on the stagnation point, Fig. 13 presents the coupled ablation results for a range of nose radii and altitude, all with a velocity of 20 km/s. Figure 13(a) presents the stagnation point radiative heating with coupled ablation divided by the case with no ablation (recall that both include coupled radiation, as have all simulations presented in this section). This “coupled ablation heating ratio” is seen to remain near a value of 0.05 below 30 km, regardless of nose radius, while above 30 km the impact of coupled ablation is less (meaning the presented ratio is closer to 1) for smaller nose radii. This results from the fact that, for a given ablation rate, the ablation product layer is thicker for larger nose radii. Below 30 km this behavior is subdued because spectral regions with strong absorption are completely

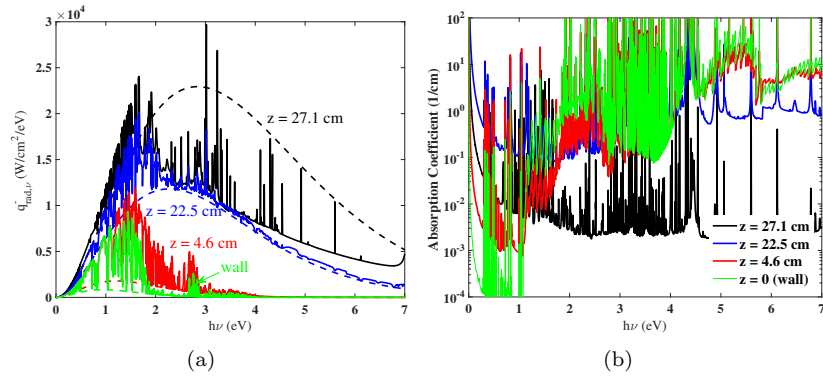


Figure 11: Spectral details at various points along the stagnation line for the 50 km altitude case.

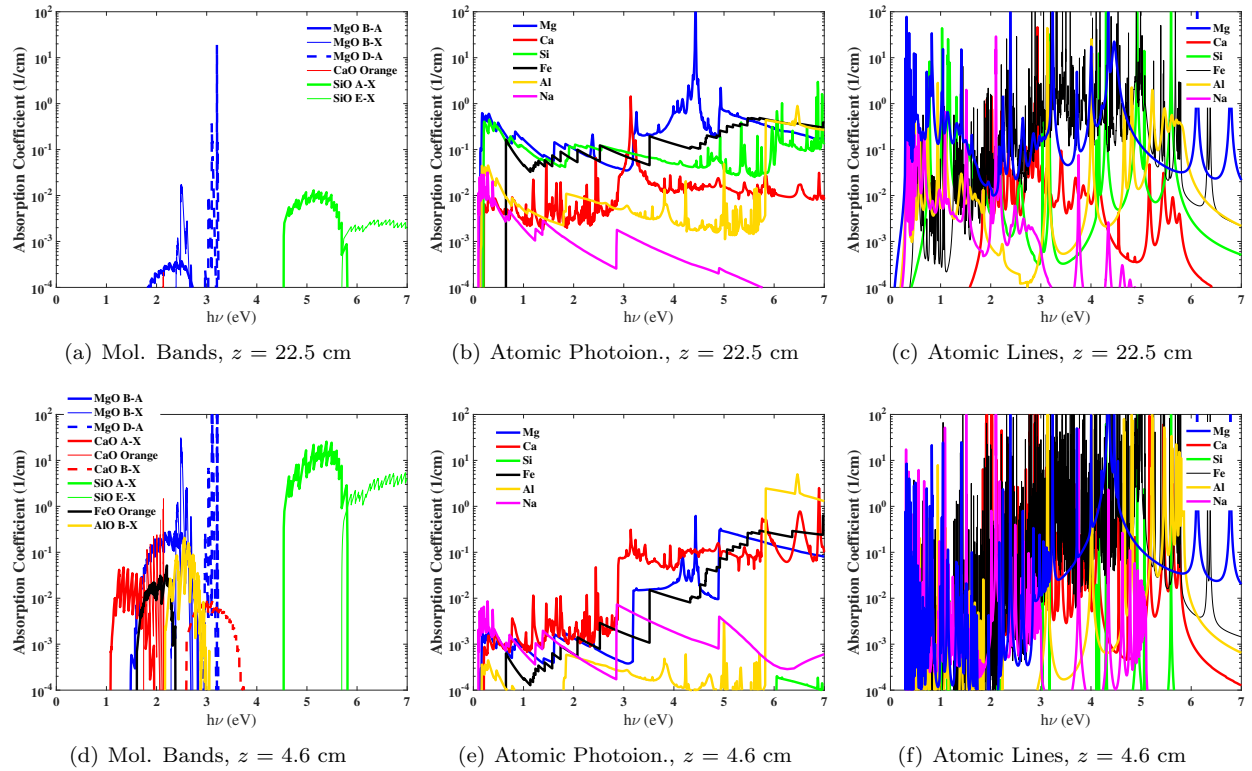


Figure 12: Spectrum components from individual species and radiative processes for the 50 km altitude case.

absorbed, resulting in the thicker absorbing ablation layer having minimal impact. Figure 13(b) presents the stagnation point radiative heating for this range of cases. Note that dividing these values by those in Fig. 4(b) will return the ratios presented in Fig. 13(a).

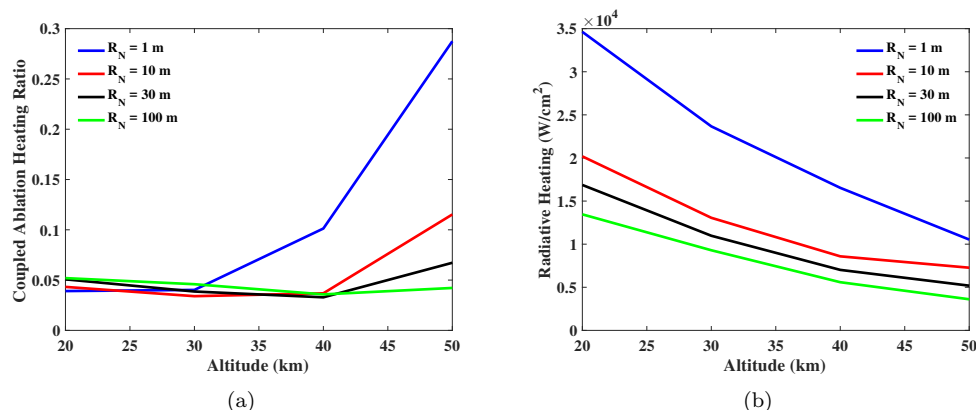


Figure 13: Impact of coupled ablation on the stagnation point at 20 km/s.

C. Impact of Turbulence

In support of the Galileo probe heatshield design for Jupiter entry, Moss et al.^{67,68} showed that turbulence had a significant impact on the radiative heating to the probe's massively ablating carbon-phenolic surface. Previous to this study, a common assumption in aerothermodynamic analyses was that turbulence had a negligible impact on radiative heating. Moss et al. showed that the higher temperatures near the surface for the turbulent case reduced the number density of the strongly absorbing C_3 molecule, which increased the radiative heating. Johnston et al.²⁹ found similar behavior for massively ablating Earth entry shock layers at 15 km/s. These studies suggest that turbulence will have a significant impact on the aerothermodynamic environment of a massively ablating meteor. The present subsection will assess this impact. Note that carbon is not present in the presently studied meteoroid composition, meaning that there is no C_3 , which provided the primary turbulence impact in the studies by Moss et al. and Johnston et al.

The present analysis applies the Cebeci-Smith turbulence model,^{69,70} with a turbulent Schmidt number of 0.9, and assumes completely turbulent flow. The presence of coupled radiation prevents the total enthalpy from being used to locate the boundary layer edge, which is required by the turbulence model. As a robust alternative, the boundary layer edge is defined as the point where the Si^+ mass fraction decreases to 5% of its peak value along a body normal line. Through trial and error, this approach was found to provide the best systematic approach for locating the boundary layer edge, in the presence of strong coupled radiation, for both mild and massive ablation rates. The application of this relatively simple turbulence model represents a feasible approach for assessing the impact of turbulence to the already complex coupled ablation and radiation simulations. The turbulent solutions are computed starting with the corresponding laminar solution. The ablation rates and wall temperatures are re-converged to the turbulent heating rates.

While this paper has so far focused exclusively on the stagnation line, the present section expands the analysis to downstream locations where the impact of turbulence is more pronounced. Note that the impact of turbulence on the stagnation point is limited because the outer-layer eddy-viscosity is proportional to the boundary layer edge velocity,⁷⁰ which is small for the stagnation line. A noticeable impact of turbulence is seen at the stagnation point, however, due to feedback from downstream regions (e.g., slight changes in the shock standoff distance at downstream locations impact the stagnation point shock standoff distance).

For the 30 km altitude case considered in previous sections, Fig. 14(a) compares the laminar and turbulent radiative heating values as a function of the radial distance from the stagnation point (the stagnation point is at 0 and the maximum radius location, or shoulder, is at 10 m). The vertical dotted line at 5.3 m defines the downstream location to be studied in subsequent figures. This figure shows that the turbulent radiative heating is up to 100% greater than the laminar values. Figure 14(b) shows that this increased radiative heating corresponds with a similar increase in the ablation rate.

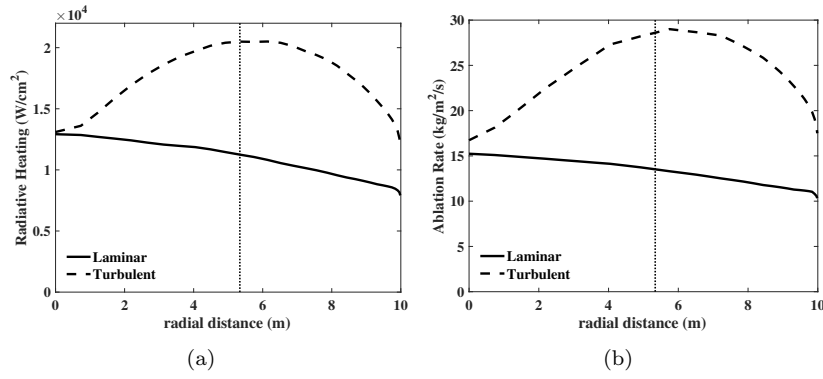


Figure 14: Impact of turbulence for the 30 km altitude case.

To determine the cause of the significant increase in the radiative heating due to turbulence, Fig. 15 compares the laminar and turbulent profiles along the body normal line indicated by the dotted line in Fig. 14. The temperatures, Si and Mg mole fractions, and q_{rad}^- profiles between the shock and wall are presented in Figs. 15 (a) - (c). These figures show the impact of turbulence on the outer region of the boundary layer, where the atomic ablation products, such as Si and Mg, are shown to diffuse further into the shock layer. The lower temperatures for the turbulent case produce lower q_{rad}^- values throughout the outer region of the boundary layer (1 - 20 cm). To clarify the details below 1 cm, Figs. 15(d) - (f) focus on the first 4 cm away from the surface. The temperatures for the turbulent case are seen to become larger than the laminar values below 1 cm. These higher temperatures are seen in Fig. 15(e) to significantly reduce the mole fractions of SiO and MgO. Absorption from MgO was shown in the previous subsection to provide significant absorption. The increased radiative heating for the turbulent case due to the reduction of MgO and CaO (which is not presented in the figure, but behaves similarly to MgO) is analogous to the reduction in C_3 predicted by Moss et al. for the Galileo probe.

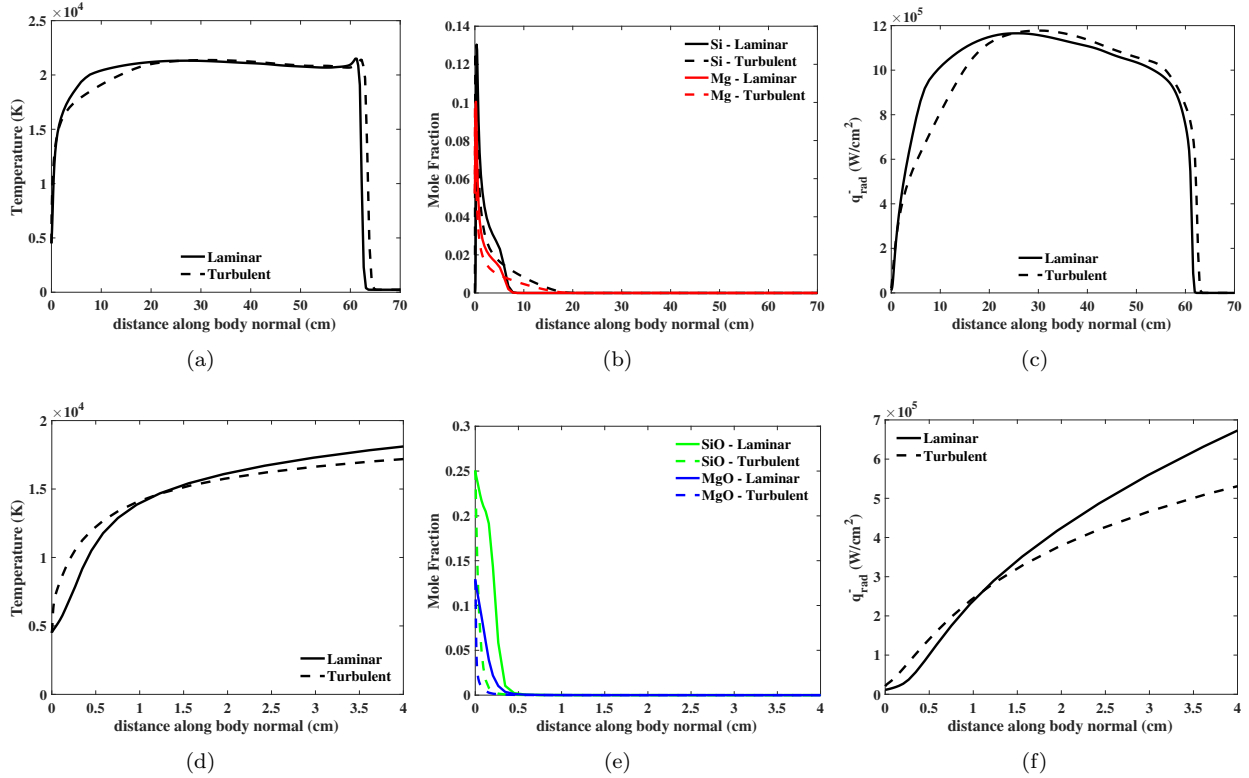


Figure 15: Impact of turbulence on the body normal line defined in Fig. 14 for the 30 km altitude case.

A similar comparison is made in Figs. 16 and 17 for the lower pressure 50 km altitude case studied in previous sections. For this case, up to a 40% increase is seen for the radiative heating and ablation rate with the addition of turbulence. Although this difference is lower than that seen for the previous higher pressure case, Fig. 17 shows that the influence of turbulence extends further into the shock layer. This is due primarily to the thicker ablation layer. As with the previous example, the temperatures for the turbulent case are higher near the surface. Again, this reduces the presence of strongly absorbing molecular species.

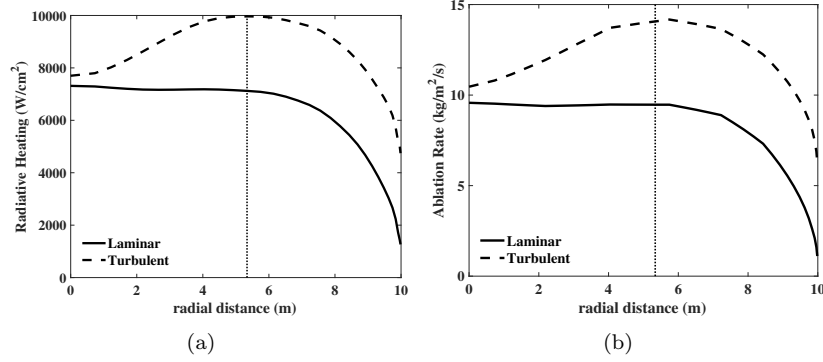


Figure 16: Impact of turbulence for the 50 km altitude case.

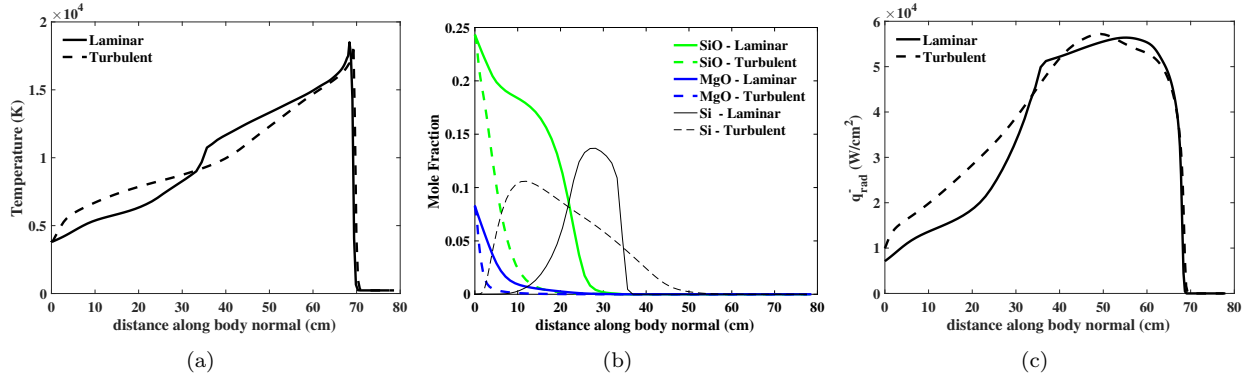


Figure 17: Impact of turbulence on the body normal line defined in Fig. 16 for the 50 km altitude case.

IV. Heat Transfer Coefficient (C_H) Model

While a primary goal of this work was to assess the impact of coupled radiation and ablation on the radiative heating to a meteoroid, the resulting simulations provide the opportunity to develop an improved model for the heat transfer coefficient (C_H). This improved C_H model may then be implemented in trajectory codes^{71–73} for simulating meteor entry. The importance of C_H , which is defined in Eq. (2), is discussed in the Introduction.

Figure 18 presents C_H values for both laminar (solid lines) and turbulent (dashed lines) flow, which all include coupled radiation and ablation. In addition to the 20 km/s cases studied throughout this paper, simulations were also performed for velocities of 14, 16, and 18 km/s. Although not shown, the impact of coupled radiation and ablation discussed throughout this paper is similar for these lower velocity cases. Figure 18 shows that the resulting C_H values are also similar for these lower velocities. The impact of turbulence, which is shown in the previous section to significantly impact the radiative heating, is seen to have a similar impact for the entire range of cases. However, even with turbulence, these C_H values remain considerably below the heritage value of 0.1. Note that this heritage value was derived by Baldwin and Sheaffer⁷⁴ based on inviscid, coupled radiation stagnation line simulations by Page et al.⁷⁵ Therefore, this heritage value of 0.1 does not include the impact of coupled ablation, which explains its overprediction relative to the present simulations.

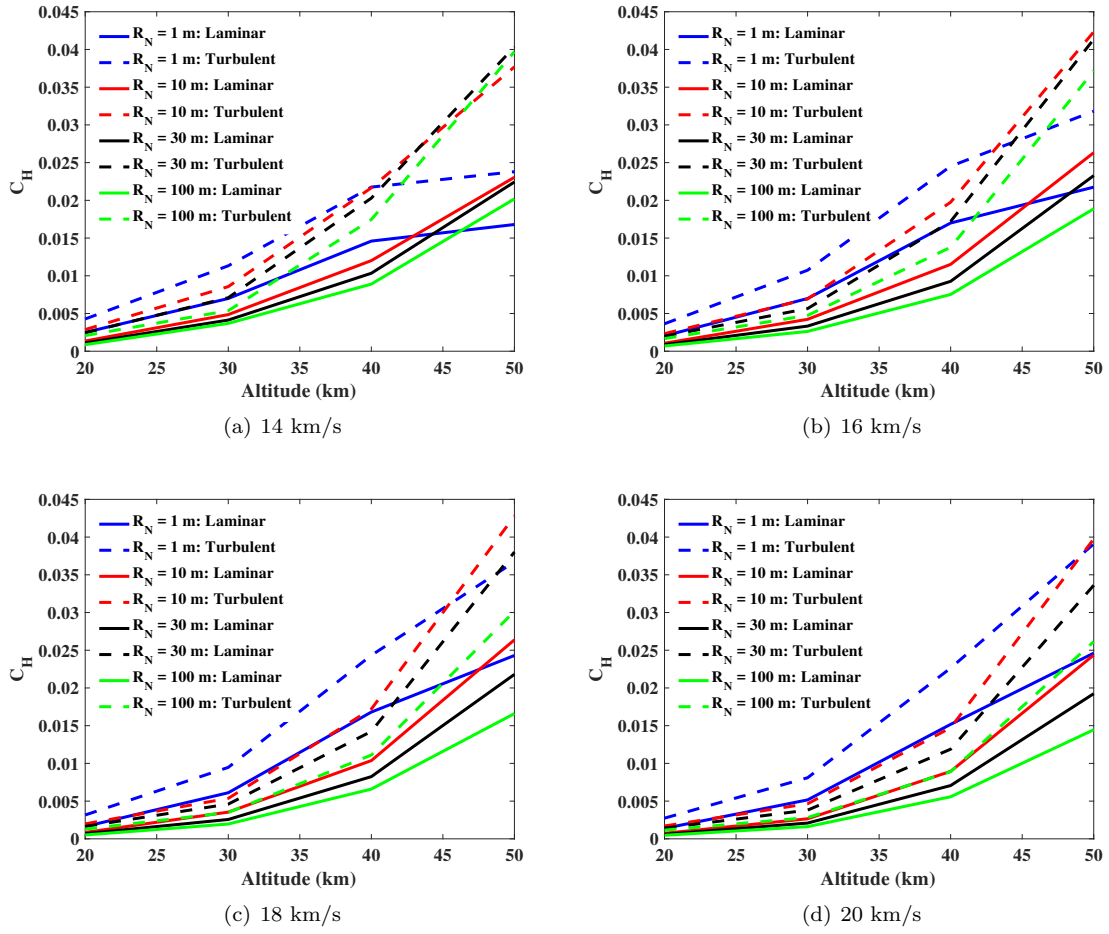


Figure 18: Coupled radiation and ablation C_H values for a range of velocities, altitudes, and nose radii.

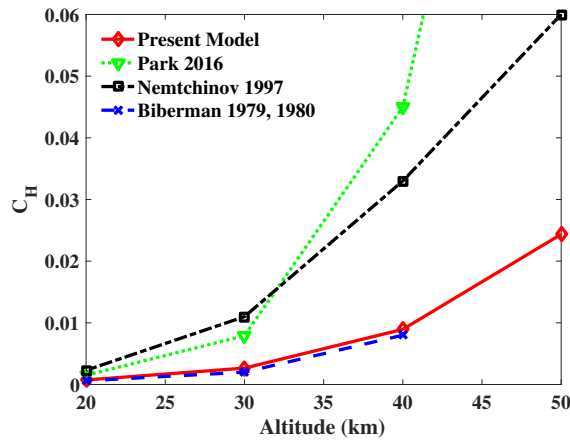


Figure 19: Comparison of C_H values at 20 km/s and $R_N = 10$ m predicted by various studies.

A comparison with C_H values presented by other researchers is presented in Fig. 19. The Park,¹⁰ Nemtchinov,⁷⁶ and Biberman^{28,77} predictions all include the impact of coupled radiation and ablation. Park applied an inviscid stagnation line analysis. The stagnation point radiative heating values presented by Park were converted to C_H values by scaling them with the present stagnation point radiative heating and C_H values. Nemtchinov applied an ablating piston flowfield model, while Biberman applied an inviscid stagnation line analysis. Note that the Biberman values are taken from the tabulated values presented by Golub et al.⁷⁸ Excellent agreement between the present results and those of Biberman is seen. The Park and Nemtchinov values, however, are more than a factor of two larger than the present results.

Because of the minimal details available regarding the Nemtchinov⁷⁶ and Biberman^{28,77} simulations, it is difficult to investigate further their comparison with the present results shown in Fig. 19. The study by Park,¹⁰ however, provides sufficient details to investigate its significantly higher C_H values. To see if this disagreement is due to differences in the applied elemental composition, h_{abl} curve-fit, or T_w curve-fit, simulations were performed using the Park values for these quantities. Park's values for h_{abl} are near 9 MJ/kg, compared to the values applied throughout this work, which are near 6.2 MJ/kg. These larger h_{abl} values result in smaller ablation rates, through Eq. (10). For T_w , Park's values are roughly 500 K lower than the present values. These values were determined by Park for an H-Chondrite, with the following elemental mass fractions: O = 0.352, Si = 0.194, Fe = 0.272, Mg = 0.159, S = 0.022. Note that Al, Ca, and Na are not included. These values for h_{abl} , T_w , and elemental composition were applied in the present simulation approach for the 30 and 50 km altitude (20 km/s and 10 m nose radius) cases studied throughout this paper. For the 30 and 50 km altitude cases, these simulations resulted in a C_H increase of 11 and 20% increase, respectively, relative to the present baseline model. These C_H values of 0.0028 and 0.029 for the 30 and 50 km cases remain a factor of three below the Park values (the Park value at 50 km is 0.16, which is off the scale in Fig. 19). It is concluded from this comparison that differences between the applied h_{abl} , T_w , and elemental composition values do not account for the differences between the present C_H values and those predicted by Park. This comparison also shows that the present C_H values are not overly sensitive to the meteoroid composition and ablation model.

V. Conclusions

A coupled radiation and ablation model is developed that treats 39 flowfield species. This includes species containing Fe, Mg, Si, Ca, Na, S, and Al. Radiation models for these atomic species, as well as their associated molecules are developed and implemented. Precursor absorption and photochemistry is included in this model, and is shown to have a negligible impact on heating below 40 km. The impact of coupled radiation is shown to reduce the radiative heating by more than 60% for meteor entries at 20 km/s with nose radii between 1 and 100 m and altitudes between 20 and 50 km. The impact of coupled radiation for optically thick shock layers, which occur below 40 km, is shown to produce two distinct layers of strong coupling near the shock and wall, which appear similar to a nonequilibrium post shock region and a large boundary layer, respectively. For the considered range of conditions, coupled ablation is shown to reduce the radiative heating by more than 70%. Absorption from Mg and MgO, along with Ca and CaO, are shown to have the largest impact on the radiative heating. Turbulence is shown to reduce the number density of strongly absorbing molecules near the surface, which is shown to result in up to a 100% increase in the radiative heating downstream of the stagnation point. Heat transfer coefficients, C_H , that include coupled radiation and ablation are computed for velocities ranging from 14 to 20 km/s, nose radii between 1 and 100 m, and altitudes between 20 and 50 km. These C_H values are lower than 0.045 for all cases, which is significantly lower than the typically assumed value of 0.1.

VI. Acknowledgments

This work was performed under the Asteroid Threat Assessment Project (ATAP), funded by the NASA Planetary Defense Coordination Office (PDCO), managed by Lindley Johnson.

References

- ¹Johnston, C. O., Samareh, J., and Brandis, A. M., "Aerothermodynamic Characteristics of 16-22 km/s Earth Entry," AIAA Paper 2015-3110, 2016.

- ²Bose, D., Brown, J. L., Prabhu, D. K., Gnoffo, P. A., Johnston, C. O., and Hollis, B. R., "Uncertainty Assessment of Hypersonic Aerothermodynamic Prediction Capability," *Journal of Spacecraft & Rockets*, Vol. 50, No. 1, 2013, pp. 12–18.
- ³Prabhu, D. K., Saunders, D., and Agrawal, P., "Thermophysics Issues Relevant to High-Speed Earth Entry of Large Asteroids," AIAA Presentation, (<https://ntrs.nasa.gov/search.jsp?R=20160000692>), 2016.
- ⁴Aftosmis, M., Nemec, M., Mathias, D. L., and Berger, M. J., "Numerical Simulation of Bolide Entry with Ground Footprint Prediction," AIAA Paper 2016–0998, 2016.
- ⁵Mathias, D. L., Wheeler, L. F., and Dotson, J. L., "A Probabilistic Asteroid Impact Risk Model: Assessment of Sub-300 m Impacts," *Icarus*, Vol. 289, 2017, pp. 106–119.
- ⁶Bronshten, V. A., *Physics of Meteoric Phenomena*, Springer, 1983.
- ⁷Popova, O. P., Jenniskens, P., and Emelyanenko, V., "Chelyabinsk Airburst, Damage Assessment, Meteorite Recovery, and Characterization," *Science*, Vol. 342, 2013, pp. 1069–1073.
- ⁸Erb, R. B., Greenshields, D. H., and Chauvin, L. T., "Apollo Thermal Protection System Development," AIAA Paper 1968–1142, 1968.
- ⁹Johnston, C. O., Gnoffo, P. A., and Sutton, K., "Influence of Ablation on Radiative Heating for Earth Entry," *Journal of Spacecraft & Rockets*, Vol. 46, No. 3, 2009, pp. 481–491.
- ¹⁰Park, C., "Inviscid-Flow Approximation of Radiative Ablation of Asteroidal Meteoroids by Line-by-Line Method," AIAA Paper 2016–0506, 2016.
- ¹¹Dias, B., Turchi, A., and Magin, T., "Stagnation-Line Simulations of Meteor Ablation," AIAA Paper 2015–2349, 2015.
- ¹²Mazaheri, A., Gnoffo, P. A., Johnston, C. O., and Kleb, B., "LAURA Users Manual," NASA TM 2010-216836, 2010.
- ¹³McBride, B. J., Zehe, M. J., and Gordon, S., "NASA Glenn Code for Calculating Coefficients for Calculating Thermodynamic Properties of Individual Species," NASA TP 2002–211556, 2002.
- ¹⁴Wright, M. J., Bose, D., Palmer, G., and Levin, E., "Recommended Collision Integrals for Transport Property Computations 1: Air Species," *AIAA Journal*, Vol. 43, No. 12, 2005, pp. 2558–2564.
- ¹⁵Wright, M. J., Hwang, H., and Schwenke, D. W., "Recommended Collision Integrals for Transport Property Computations Part 2: Mars and Venus Entries," *AIAA Journal*, Vol. 45, No. 1, 2007, pp. 281–288.
- ¹⁶Svehla, R. A., "Estimated Viscosities and Thermal Conductivities of Gases at High Temperatures," NASA TR R 142, 1962.
- ¹⁷Park, C., Jaffe, R. L., and Partridge, H., "Chemical-Kinetic Parameters of Hyperbolic Earth Entry," *Journal of Thermophysics and Heat Transfer*, Vol. 15, No. 1, 2001, pp. 76–90.
- ¹⁸Johnston, C. O., Gnoffo, P. A., and Mazaheri, A., "Influence of Coupled Radiation and Ablation on the Aerothermodynamic Environment of Planetary Entry Vehicles," VKI Lecture STO-AVT-218, 2013.
- ¹⁹Johnston, C. O., Hollis, B. R., and Sutton, K., "Spectrum Modeling for Air Shock-Layer Radiation at Lunar-Return Conditions," *Journal of Spacecraft & Rockets*, Vol. 45, Sep.-Oct. 2008, pp. 865–878.
- ²⁰Johnston, C. O., Hollis, B., and Sutton, K., "Non-Boltzmann Modeling for Air Shock Layers at Lunar Return Conditions," *Journal of Spacecraft & Rockets*, Vol. 45, Sep.-Oct. 2008, pp. 879–890.
- ²¹Johnston, C. O., Brandis, A. M., and Bose, D., "Radiative Heating Uncertainty for Hyperbolic Earth Entry, Part 3: Comparisons with EAST Measurements," *Journal of Spacecraft & Rockets*, Vol. 50, No. 1, 2013, pp. 48–55.
- ²²Johnston, C. O., Sutton, K., Prabhu, D., and Bose, D., "Radiative Heating Uncertainty for Hyperbolic Earth Entry, Part 2: Comparisons with 1960s Era Shock Tube Measurements," *Journal of Spacecraft & Rockets*, Vol. 50, No. 1, 2013, pp. 39–47.
- ²³Brandis, A. M., Johnston, C. O., Cruden, B. A., Prabhu, D. K., and Bose, D., "Validation of High Speed Earth Atmospheric Entry Radiative Heating from 9.5 to 15.5 km/s," AIAA Paper 2012–2865, 2012.
- ²⁴Gnoffo, P. A., Johnston, C. O., and Thompson, R. A., "Implementation of Radiation, Ablation, and Free-Energy Minimization in Hypersonic Simulations," *Journal of Spacecraft & Rockets*, Vol. 47, No. 2, 2010, pp. 481–491.
- ²⁵Johnston, C. O. and Mazaheri, A., "Impact of Non-Tangent-Slab Radiative Transport on Flowfield-Radiation Coupling," AIAA Paper 2017–1371, 2017.
- ²⁶Goulard, R., "The Coupling of Radiation and Convection in Detached Shock Layers," *Journal of Quantitative Spectroscopy and Radiative Transfer*, Vol. 1, 1961, pp. 249–257.
- ²⁷Goulard, R., "Preliminary Estimates of Radiative Transfer Effects on Detached Shock Layers," *AIAA Journal*, Vol. 2, No. 3, 1964, pp. 494–502.
- ²⁸Biberman, L. M., Ronin, S. Y., and Brykin, M. V., "Moving of a Blunt Body through the Dense Atmosphere under Conditions of Severe Aerodynamic Heating and Ablation," *Acta Astronautica*, Vol. 7, No. 1, 1980, pp. 53–65.
- ²⁹Johnston, C. O., Mazaheri, A., Gnoffo, P., Kleb, B., and Bose, D., "Radiative Heating Uncertainty for Hyperbolic Earth Entry, Part 1: Flight Simulation Modeling and Uncertainty," *Journal of Spacecraft & Rockets*, Vol. 50, No. 1, 2013, pp. 19–38.
- ³⁰Stanley, S. A. and Carlson, L. A., "Effects of Shock Wave Precursor Ahead of Hypersonic Entry Vehicles," *Journal of Spacecraft & Rockets*, Vol. 29, No. 2, 1992, pp. 190–197.
- ³¹Mnatsakanyan, A. K., "Photodissociation and Photoionization of Diatomic Molecules at High Temperatures," *High Temperature*, Vol. 6, 1968, pp. 230–235.
- ³²Romanov, G. S., Stankevich, Y. A., Stanchits, L. K., and Stepanov, K. L., "Thermodynamic and Optical Properties of Gases in a Wide Range of Parameters," *International Journal of Heat and Mass Transfer*, Vol. 38, No. 3, 1995, pp. 545–556.
- ³³Cunto, W., Mendoza, C., Ochsenbein, F., and Zeippen, C., "TOPbase at the CDS," *Astronomy and Astrophysics*, Vol. 275, Aug. 1993, pp. L5–L8, see also vizier.u-strasbg.fr/topbase/topbase.html.
- ³⁴Gnoffo, P. A., Gupta, R. N., and Shinn, J. L., "Conservation Equations and Physical Models for Hypersonic Air Flows in Thermal and Chemical Nonequilibrium," NASA TP 2867, Feb. 1989.
- ³⁵Chen, Y.-K., "Thermal Ablation Modeling for Silicate Materials," AIAA Paper 2016–1514, 2016.
- ³⁶Gordon, S. and McBride, B. J., "Thermodynamic Data to 20,000 K for Monatomic Gases," NASA TP 1999–208523, 1999.

- ³⁷Park, C., Howe, J. T., Jaffe, R. L., and Candler, G. V., "Review of Chemical-Kinetic Problems for Future NASA Missions, II: Mars Entries," *Journal of Thermophysics and Heat Transfer*, Vol. 8, No. 1, 1994, pp. 9–23.
- ³⁸Mick, H.-J., Burmeister, M., and Roth, P., "Atomic Resonance Absorption Spectroscopy Measurements on High-Temperature CO Dissociation Kinetics," *AIAA Journal*, Vol. 31, No. 4, 1993, pp. 671–676.
- ³⁹Picard, S. D. L., Canosa, A., Reignier, D., and Stoecklin, T., "A Comparative Study of the Reactivity of the Silicon Atom Si Towards O₂ and NO Molecules at Very Low Temperatures," *Physical Chemistry Chemical Physics*, Vol. 4, 2002, pp. 3659–3664.
- ⁴⁰Akhmadov, U. S., Zaslanko, I. S., and Smirnov, V. N., "Mechanism and Kinetics of Interaction of Fe, Cr, Mo, and Mn," *Kinetics and Catalysis*, Vol. 29, 1988.
- ⁴¹Hodgson, A. and Mackie, J., "A Shock Tube Study of the Kinetics of Evaporation and Oxidation of Magnesium," *Combustion and Flames*, Vol. 35, 1979.
- ⁴²Lu, C. W., Wu, Y. J., Lee, Y. P., Zhu, R. S., and Lin, M. C., "Experiments and calculations on rate coefficients for pyrolysis of SO₂ and the reaction O plus SO at high temperatures," *Journal of Physical Chemistry A*, Vol. 107, 2002, pp. 11020–11029.
- ⁴³Murakami, Y., Onishi, S., Kobayashi, T., Fujii, N., Isshiki, N., Tsuchiya, K., Tezaki, A., and Matsui, H., "High temperature reaction of S+SO₂ = SO+SO: Implication of S₂O₂," *Journal of Physical Chemistry A*, Vol. 107, 2003, pp. 10996 – 11000.
- ⁴⁴Garland, N. L., "Temperature dependence of the reaction: SO + O₂," *Chemical Physics Letters*, Vol. 290, 1998, pp. 385 – 390.
- ⁴⁵Cohen, N. and Westberg, K. R., "Chemical Kinetic Data Sheets for High-Temperature Chemical Reactions," *Journal of Physical and Chemical Reference Data*, Vol. 12, 1983.
- ⁴⁶Fontijn, A. and Felder, W., "HTFFR kinetics studies of the Al/SO₂ reaction from 700 to 1600 K. Implications for D(Al-O)," *Journal of Chemical Physics*, Vol. 71, 1979.
- ⁴⁷Plane, J. M. C. and Husain, D., "Determination of the absolute rate constant for the reaction O+NaO = Na+O₂ by time-resolved atomic chemiluminescence," *J. Chem. Soc. Faraday Trans. 2*, Vol. 82, 1986, pp. 2047 – 2052.
- ⁴⁸Kashirenin, O. E., Kuznetsov, V. A., and Manelis, G. B., "Kinetics of alkaline-earth atoms reactions with molecular oxygen," *AIAA Journal*, Vol. 15, 1977, pp. 1035 – 1037.
- ⁴⁹Griem, H. R., *Spectral Line Broadening by Plasmas*, Academic Press, New York, 1974.
- ⁵⁰Park, C., "Rosseland Mean Opacities of Air and H-Chondrite Vapor in Meteor Entry Problems," *Journal of Quantitative Spectroscopy and Radiative Transfer*, Vol. 127, 2013, pp. 158–164.
- ⁵¹Geier, M., Dreyer, C. B., and Parker, T. E., "Laser-Induced Emission Spectrum from High-Temperature Silica-Generating Flames," *Journal of Quantitative Spectroscopy and Radiative Transfer*, Vol. 109, 2008, pp. 822–830.
- ⁵²Park, C. and Arnold, J. O., "A Shock-Tube Determination of the SiO (A¹Π – X¹Σ⁺) Transition Moment," *Journal of Quantitative Spectroscopy and Radiative Transfer*, Vol. 19, 1978, pp. 1–10.
- ⁵³Naidu, G. T., Reddy, R. R., and Rao, T. V. R., "r-Centroids and Franck-Condon Factors of the SiO Molecule," *Physica C*, Vol. 106, 1981, pp. 308–310.
- ⁵⁴Drira, I., Spielfiedel, A., Edwards, S., and Feautrier, N., "Theoretical Study of the A¹Π – X¹Σ⁺ and E¹Σ⁺ – X¹Σ⁺ Bands of SiO," *Journal of Quantitative Spectroscopy and Radiative Transfer*, Vol. 60, 1998, pp. 1–8.
- ⁵⁵Lagerqvist, A., Renhorn, I., and Elander, N., "The Spectrum of SiO in the Vacuum Ultraviolet Region," *Journal of Molecular Spectroscopy*, Vol. 46, 1973, pp. 285–315.
- ⁵⁶Michels, H. H., "Theoretical Determination of Metal Oxide f Numbers," AFWL-TR 74-239, 1975.
- ⁵⁷Daily, J. W., Drewier, C., Abbud-Madrid, A., and Branch, M. C., "Transition Probabilities in the B¹Σ⁺ – A¹Π Electronic Systems of MgO," *Journal of Molecular Spectroscopy*, Vol. 214, 2002, pp. 111–116.
- ⁵⁸Bell, R. A., Dwivedi, P. H., Branch, D., and Huffaker, J. N., "Rotational Dependence of Franck-Condon Factors for Selected Band Systems of TiO, ZrO, MgO, LaO, and SiO," *Astrophysical Journal Supplement Series*, Vol. 41, 1979, pp. 593–630.
- ⁵⁹Naulin, C., Costes, M., Moudden, Z., and Dorthe, G., "Measurements of the Radiative Lifetimes of MgO (B,d,D) States," *Chemical Physics Letters*, Vol. 2, 1991, pp. 325–329.
- ⁶⁰Doherty, P. H., Midey, A. J., Miller, T. M., Levandier, D. J., Holeman, E., Webb, D. F., and Martin, K., "Comprehensive Methods for Determining Space Effects on Air Force Systems," AFRL-RV-HA-TR 2009-1100, 2009.
- ⁶¹Liszt, H. S. and Smith, W. H., "RKR Franck-Condon Factors for Blue and Ultraviolet Transitions of some Metal Oxides," *Journal of Quantitative Spectroscopy and Radiative Transfer*, Vol. 11, 1971, pp. 1043–1062.
- ⁶²Pasternack, L. and Dagdigan, P. J., "The Reaction of Metastable Ca Atoms with O₂ and CO₂," *Chemical Physics*, Vol. 33, 1978, pp. 1–11.
- ⁶³Baldwin, D. P. and Field, R. W., "The Green-Band Transitions of CaO," *Journal of Molecular Spectroscopy*, Vol. 139, 1990, pp. 68–76.
- ⁶⁴Borin, A. C. and Ornellas, F. R., "A Theoretical Investigation of the A³Π-X³Σ⁻ Transition in SO," *Chemical Physics Letter*, Vol. 322, 2000, pp. 149–156.
- ⁶⁵Rosen, B., *Spectroscopic Data Relative to Diatomic Molecules*, Pergamon Press, 1970.
- ⁶⁶Borovicka, J. and Berezhnoy, A. A., "Radiation of Molecules in Benesov Bolide Spectra," *Icarus*, Vol. 278, 2016, pp. 248–265.
- ⁶⁷Moss, J. N. and Simmonds, A. L., "Galileo Probe Forebody Flowfield Predictions During Jupiter Entry," AIAA Paper 1982-0874, 1982.
- ⁶⁸Moss, J. N., Simmonds, A. L., and Anderson, E. C., "Turbulent Radiating Shock Layers with Coupled Ablation Injection," *Journal of Spacecraft & Rockets*, Vol. 17, No. 3, 1980, pp. 177–183.

- ⁶⁹Cebeci, T., "Variation of the Van Driest Damping Parameter with Mass Transfer," *AIAA Journal*, Vol. 11, No. 2, 1973, pp. 237–238.
- ⁷⁰Cheatwood, F. M. and Thompson, R. A., "The Addition of Algebraic Turbulence Modeling to Program LAURA," NASA TM 107758, 1993.
- ⁷¹Revelle, D. O., "Recent Advances in Bolide Entry Modeling: A Bolide Potpourri," *Earth*, Vol. 95, No. 1, Dec. 2004, pp. 441–476.
- ⁷²Hills, J. G. and Goda, M. P., "The fragmentation of small asteroids in the atmosphere," *Astronomical Journal (ISSN 0004-6256)*, Vol. 105, March 1993, pp. 1114–1144.
- ⁷³Wheeler, L. F., Register, P. J., and Mathias, D. L., "A fragment-cloud model for asteroid breakup and atmospheric energy deposition," *Icarus*, Feb. 2017, pp. 1–21.
- ⁷⁴Baldwin, B. and Sheaffer, Y., "Ablation and Breakup of Large Meteoroids during Atmospheric Entry," *Journal of Geophysical Research*, Vol. 76, 1971, pp. 4653–4666.
- ⁷⁵Page, W. A., Compton, D. L., Borucki, W. J., Cifone, D. L., and Cooper, D. M., "Thermal Ablation Modeling for Silicate Materials," AIAA Paper 68–784, 1968.
- ⁷⁶Nemchinov, I. V., Svetsov, V. V., Kosarev, I. B., Golub, A. P., Popova, O. P., and Shuvalov, V. V., "Assessment of Kinetic Energy of Meteoroids Detected by Satellite-Based Light Sensors," *Icarus*, Vol. 130, 1997, pp. 259–274.
- ⁷⁷Biberman, L. M., Bronin, S. Y., and Brykin, M. V., "Heat Transfer in Hypersonic Flow with Strong Radiative Convective Interaction," *High Temperature*, Vol. 17, 1979, pp. 84–91.
- ⁷⁸Golub, A. P., Kosarev, I. B., Nemchinov, I. V., and Shuvalov, V. V., "Emission and Ablation of a Large Meteoroid in the Course of Its Motion Through the Earth's Atmosphere," *Solar System Research*, Vol. 30, No. 3, 1996, pp. 213–228.